

Research paper

Optimal declutching control of hinged multiple floating bodies

Shuang-Rui Yu ^a, Ming Zhang ^{a,*}, De-Qing Zhang ^{a,b}, Zhi-Ming Yuan ^a^a Department of Naval Architecture, Ocean and Marine Engineering, University of Strathclyde, Glasgow, G4 0LZ, UK^b College of Engineering, Ocean University of China, Qingdao, 266100, PR China

ARTICLE INFO

Keywords:

Multi-body hydrodynamics
Optimal control
Declutching control
Pontryagin's maximum principle
Power take off (PTO)

ABSTRACT

In deep seas, there is an increasing utilisation of multiple floating structures as devices for harnessing renewable energy, such as hybrid wind-wave energy systems and multi-body wave energy converters. The control strategies have a great influence on the motion characteristics and energy conversion efficiency of these systems. The control technology brings more benefits to the system's performance, yet also introduces more complex challenges. This paper aims to fill the research gap in the control of multiple floating bodies and to propose a novel optimal declutching control method. Declutching control enables discontinuous loading and releasing of the force from power take-off system between bodies. It was found that the feasibility of the proposed method is highly dependent on the choice of objective functions, iteration numbers, and wave frequencies. With appropriate parameters, the declutching control can achieve a variety of objectives for a hinged floating multibody system, such as reducing pitch motion, improving extracted wave power, increasing relative rotational speed, and enhancing power extraction. The control effects on the velocity and the force-velocity phase relationship and how they benefit the objectives are discussed. All objective functions show a better control effect (at least 7.76%) on their respective performance indices than others.

1. Introduction

Floating structures are increasingly used to harness renewable energy in deep seas. To enhance energy absorption efficiency, a notable trend is designing these devices as floating multi-body systems. This concept is often implemented in the form of hybrid systems or modular configurations. Floating multibody arrays are widely applied in floating offshore wind turbine (e.g., Spar-Torus Combination concept (Muliawan et al., 2013)) and wave energy converter arrays (e.g., Pelamis (Henderson, 2006; Yemm et al., 2012)), floating airports and bridges (e.g., Bergsøysund bridge (Cheng et al., 2018)), and floating photovoltaic systems (e.g., Zon-op-Zee). These structures are composed of individual floating bodies, with or without connection among them. Their dynamic behaviours under operational conditions are affected by the hydrodynamic interactions with the surrounding waves or between the bodies.

For multiple floating bodies, the existing research has mainly focused on the hydrodynamics interactions (Zhang et al., 2023), not involving the effect of control algorithms. This paper has found that various objectives can be achieved through the implementation of control methods. We specifically investigate the control strategies aimed at mitigating the negative effects of motion on the stability of a multibody

system, or enhancing the power output of the system. Previous studies are summarised in a sequence of 1.1 Single body control and 1.2 Multibody hydrodynamic interactions. The novelty of this paper is then presented in subsection 1.3.

1.1. Single body control

Various Wave Energy Converters (WECs) are designed to maximise the absorption of wave energy and convert it into kinetic or potential energy, which is then converted into electric energy by Power Take Off (PTO) devices. For a single-body WEC, such as the heaving point absorber WEC, there are various control strategies proposed to maximise the energy output (Ringwood et al., 2014). Among them, phase control is a simple but effective control method to tune the phase between the body velocity and the wave force. Latching control and declutching control are two complementary methods in phase control. Their control commands are both binary functions. Latching control provides an infinite damping force alternatively by locking and releasing the floating body with a brake system. The braking effect is similar to a car hand-brake, where the brake is applied at zero velocity and reliance is made on static friction to prevent motion (Ringwood et al., 2014). Declutching

* Corresponding author.

E-mail addresses: ming.zhang.100@strath.ac.uk, zhangming920123@163.com (M. Zhang).

control system provides discrete damping force by switching on and off alternatively the by-pass valve in the circuit of the hydraulic cylinder. For floating bodies with a connection to the seabed, like point absorber buoys, latching control can be easily realised by devices like a brake mechanism that can increase the damping instantly. Nevertheless, for floating bodies without connection to the seabed, providing latching force presents significant challenges. Latching control only locks the multiple bodies together. Therefore, it cannot keep the bodies static and perfectly tune the system's phase.

Declutching control is a necessary solution to complement the latching control for floating multiple hinged bodies, and is typically implemented in conjunction with PTO systems. The concept of declutching control or unlatching control was introduced in (Salter et al., 2002) as a complement of latching control. The declutching control means switching on and off alternatively the by-pass valve in the circuit of the hydraulic cylinder. When declutching happens, the by-pass valve is switched on and the damping force is set equal to 0. Babarit et al. (2009) compared declutching control with pseudo-continuous control, a method realised by deploying several hydraulic cylinders and/or several high-pressure accumulators with different pressure levels in the PTO system. Declutching control is proven to have even higher energy absorption while its control device is simpler. After comparing different control strategies for a sphere WEC, Hals et al. (2011) also determined that latching and declutching control strategies are attractive because of their simplicity and because they do not require additional energy input. In the research of Zhang et al. (2014) on a hemispherical WEC, the amplification ratio of absorbed power by declutching control is less than 1.1. It indicates that declutching control is inapplicable for oscillating WEC in proposed wave frequencies in this research. The analysis of declutching control on a single body shows a distinct relationship with wave frequency, which may vary in the case of multiple floating bodies.

1.2. Multi-body hydrodynamic interactions

Numerical methods for solving hydrodynamic interaction have been developed for decades. Choi and Hong (2002) used a high-order boundary element method (BEM) to compute the hydrodynamic parameters of floating multi-body and compared the numerical results with model test results. The results both showed that the hydrodynamic parameters of a floating multi-body system are very different from a single floating body due to the interaction between bodies. Yuan et al. (2015) developed a 3-D Rankine source method to investigate the hydrodynamic interactions between two travelling ships. Their computational results gave a good agreement with the experimental results conducted by Kashiwagi et al. (2005). Zhang et al. (2022) extended Yuan's method (Yuan et al., 2015) by introducing a cut-off radius to analyse the radiated hydrodynamic coefficients of a multi-box array. Their numerical results showed that it is feasible to model the hydrodynamic properties of large arrays of floating bodies. The cut-off range method significantly reduces computational time when simulating the interaction between multiple floating bodies.

Compared to the hydrodynamic coefficients, the motion interactions of the floaters have a more direct impact on the performance of WECs. Moreover, the hinge constraints among these devices can significantly change their responses. Published studies have proposed several methods for solving the motion responses of hinged multi-body systems. Newman (1994) first took hinge constraints into consideration in multi-body problems. He utilised a mode generalized method to predict the vertical motion and relative rotation of a hinge in a two-barge system. Sun et al. (2011) applied the Lagrange multiplier technique to investigate the same interconnected barge configuration. They compared their numerical results with Newman's results and got a good agreement. Zheng et al. (2015) used the method of introducing a constraint matrix in the frequency-domain dynamic equation to calculate the motion results. Their results also agreed well with the results from Newman's method (Newman, 1994). Noad and Porter (2017)

compared device proportions, hinge position and number of pontoons of an articulated raft WEC. They found that placing longer pontoons to the aft is beneficial to the power performance of system.

However, more research is needed on the application of the constraint matrix method in the time domain. Zheng et al. (2015) carried out a time-domain analysis of a raft-type WEC to investigate the mechanism and effect of latching control. They compared the parameters of the cylindrical raft and the PTO damping coefficients to maximise the power capture. Even at optimal parameters and damping coefficient, there are phase lags between wave excitation moments and velocities in the pitch direction. These lags can be eliminated by non-uniform mass distribution or latching control in certain wave conditions. Pelamis (Henderson, 2006; Yemm et al., 2012) was designed to absorb wave energy from the rotational motion between 4 and 5 tube segments and its dynamics show good energy capture efficiency and extreme wave condition resistance. The control algorithms allow the performance improvement of floating multiple bodies in the time domain. Zhou et al. (2023) built a time-domain model of hinged WEC with negative stiffness mechanism (NSM) and verified the model in experiment. The NSM can increase the pitch response of a two-module WEC by as much as 60%. Li et al. (2021) implemented a real-time declutching control to a bi-oscillator WEC to enhance power capture. This research focuses on the implementation of the developed wave force prediction algorithm based on artificial neural networks and power extraction. The power absorption is significantly enhanced; however, the motion of the outer oscillator is not well analysed. Liu et al. (2022) proposed a discrete control method based on discrete control force by switching the valves in the hydraulic PTO system. The combination of declutching control and load control shows a good performance enhancement in the entire wave bandwidth. In research applying declutching control to the multi-body systems, the main purpose is to maximise the electric power generation of WEC. In this paper, however, more physical scenarios and objectives are applied to the control of floating multiple bodies.

1.3. Objective of this paper

In summary, most of the published works are either focused on single-body control or multi-body hydrodynamic interactions. There are very limited published works on the control of multiple floating bodies. The application of declutching control to multiple floating bodies has rarely been studied. Moreover, whether declutching control is applicable to different objectives, such as reducing the motion of one body in a multi-body system, has not been investigated.

In this paper, the hydrodynamics and declutching control effects of a hinged multiple floating bodies system will be systematically studied. The hinged barges in Newman's research (Newman, 1994) are selected as the model to investigate the relationship between their velocities and the wave forces or moments. The declutching control is realised by the PTO device, which could provide a discrete damping force as the control force. The discontinuity in the control force introduces additional nonlinearity into the system. Different objective functions are developed to realise different control effect goals with declutching optimal control. The time-domain control results of declutching optimal control are analysed to show the control effect. The influences of iteration, error threshold, and wave frequency in the optimal control algorithm are also discussed.

Section 2 establishes a hydrodynamic model of the hinged floating multi-body system. Section 3 introduces optimal declutching control applied in this paper, including the mechanism of declutching control and the algorithm of optimal control using Pontryagin's Maximum Principle (PMP). Section 4 presents motion and power absorption results with the developed control method. Control effect and influence factors are discussed herein.

2. Hydrodynamic modelling of multiple floating bodies

2.1. Time-domain hydrodynamic model

In this section, the theoretical model is an extension of the typical hinged-box system deployed in Newman's research (Newman, 1994). The configuration of N rectangular boxes of equal size is depicted in Fig. 1. The global coordinate $o\text{-}xyz$ is a right-handed Cartesian coordinate with $x\text{-}y$ axes in the horizontal water plane and z axis oriented in the upward direction. The boxes have a uniform mass distribution so that their centres of gravity (CoG) are located at the water surface. The water depth, h , is assumed to be infinite, and the waves are propagating towards the positive x -axis throughout the computation. The motion responses are described in body-fixed coordinates $o^j\text{-}x^jy^jz^j$, where j corresponds to the j -th body.

Assuming the flow field is ideal, potential flow theory is applied to derive the hydrodynamic coefficients of the floating bodies. For a multi-body floating system, the dimensions of the mass matrix, motion vector, and force vector are $6N \times 6N$, $6N \times 1$, and $6N \times 1$ respectively, where N is the number of bodies. The motion equation of the N -body system is as follows

$$(\mathbf{M} + \mathbf{m})\ddot{\boldsymbol{\eta}}(t) + \int_0^t \mathbf{h}_r(t - \tau) \dot{\boldsymbol{\eta}}(\tau) d\tau + \mathbf{K}\boldsymbol{\eta}(t) = \mathbf{f}_e(t) + \mathbf{f}_{\text{PTO}}(t) \quad (1)$$

where the hydrodynamic coefficients and excitation wave forces are described in their body-fixed coordinates respectively. \mathbf{M} is the body mass matrix; $\mathbf{h}_r(t)$ is the kernel retardation function matrix; \mathbf{K} is the stiffness matrix; $\boldsymbol{\eta}(t)$, $\dot{\boldsymbol{\eta}}(t)$ and $\ddot{\boldsymbol{\eta}}(t)$ are the position, velocity and acceleration vectors respectively, where $\boldsymbol{\eta} = [\eta_1^1, \eta_1^2, \dots, \eta_1^N]^T$, $i = 1, 2, \dots, 6$; $\mathbf{f}_e(t)$ is the wave excitation force vector; $\mathbf{f}_{\text{PTO}}(t)$ is the PTO damping force vector between adjacent multiple floating bodies.

In studies of wave motion on the surface of a fluid, it is common to assume that the amplitudes of the waves are small compared to the wavelengths. For simplicity, a regular wave can be assumed to be sinusoidal with constant wave amplitude, wavelength, and wave period.

Thus, $\mathbf{f}_e(t)$ can be expressed as sinusoidal functions

$$f_{e,i}(t) = \zeta^A f_W \cos(\omega t + \varepsilon_i), i = 1 \sim 6 \quad (2)$$

where $f_{e,i}(t)$ is the i -th component of $\mathbf{f}_e(t)$; f_W is the wave force transfer function calculated by the commercial potential flow theory software WADAM using the multi-box model; ζ^A is the incoming wave amplitude; ω is the angular wave frequency; ε_i are the phases of harmonic components of a periodic wave. The PTO force is defined as

$$f_{\text{PTO}}^j(t) = -B_{\text{PTO}}\Delta\dot{\theta}^j(t), j = 1, 2, \dots, N - 1 \quad (3)$$

where B_{PTO} is the PTO damping, which is defined as a constant; $\Delta\dot{\theta}^j(t)$ is the relative angular velocity between the adjacent j -th and $(j+1)$ -th floating bodies. The average power output of the system's PTO is defined as

$$P_{\text{PTO}} = \frac{1}{T_2 - T_1} \int_{T_1}^{T_2} \left(\sum_{j=1}^{N-1} B_{\text{PTO}} \Delta\dot{\theta}^j(t)^2 \right) dt \quad (4)$$

where t is time and $T_2 - T_1$ is the length of selected time horizon; $\int_0^t \mathbf{h}_r(t - \tau) \dot{\boldsymbol{\eta}}(\tau) d\tau$ is the convolution integral expression of radiation force. It can be approximated and expressed with state-space representation, which is discussed in detail in Section 2.2.

In this paper, two floating bodies are considered as an example, and hence, N is set to be 2 herein. The hydrodynamics of the hinged-box system was discussed in Newman's research (Newman, 1994). The motion equation (1) of the two-body system is a 12-DoF (Degree of Freedom) equation, where $\boldsymbol{\eta} = [\eta_1^1, \eta_1^2]^T$, $i = 1, 2, \dots, 6$ or represented as $\boldsymbol{\eta} = [x^1, y^1, z^1, \varphi^1, \theta^1, \psi^1, x^2, y^2, z^2, \varphi^2, \theta^2, \psi^2]^T$, representing surge, sway, heave, roll, pitch, and yaw respectively; $f_{\text{PTO}} = -B_{\text{PTO}}\Delta\dot{\theta}(t)$, where $\Delta\dot{\theta}(t)$ is the relative angular velocity between *Box_1* and *Box_2* herein.

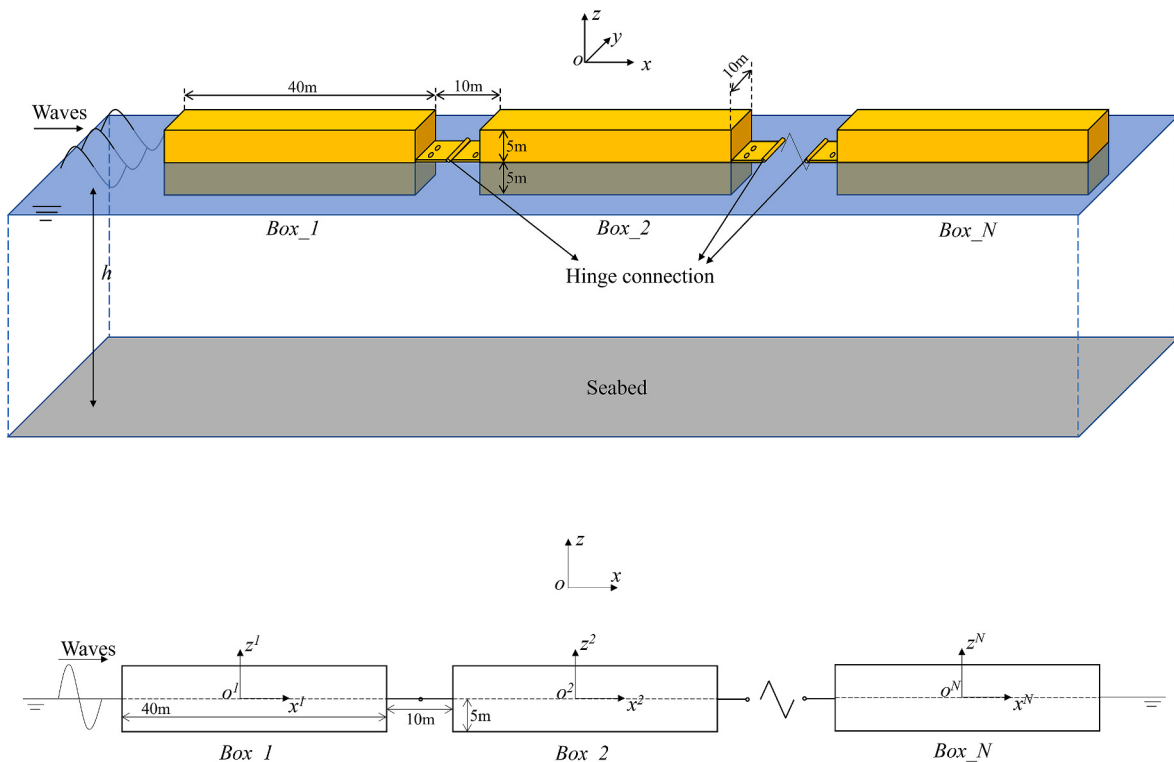


Fig. 1. Configuration of hinged boxes.

2.2. Impulse response theory

In the time domain, the nonlinear radiation term in the motion equations can be derived from Cummins' impulse response theory (Cummins, 1962). According to Cummins' equation, the radiation force is expressed as follows

$$\mathbf{f}^R(t) = \int_0^t \mathbf{h}_r(t-\tau) \dot{\eta}(\tau) d\tau \quad (5)$$

$\mathbf{h}_r(t)$ can be obtained from the added mass $\mu(\omega)$ or the potential

$$\begin{aligned} \begin{bmatrix} \mathbf{M}^1 + \mathbf{m}^1 & \mathbf{m}^{12} \\ \mathbf{m}^{21} & \mathbf{M}^2 + \mathbf{m}^2 \end{bmatrix} \begin{bmatrix} \ddot{\eta}^1 \\ \ddot{\eta}^2 \end{bmatrix} + \begin{bmatrix} \mathbf{C}_r^1 & \mathbf{C}_r^{12} & \mathbf{0} & \mathbf{0} \\ \mathbf{0} & \mathbf{0} & \mathbf{C}_r^2 & \mathbf{C}_r^{21} \end{bmatrix} \begin{bmatrix} \mathbf{u}^1 \\ \mathbf{u}^{12} \\ \mathbf{u}^2 \\ \mathbf{u}^{21} \end{bmatrix} + \begin{bmatrix} \mathbf{K}^1 & \mathbf{0} \\ \mathbf{0} & \mathbf{K}^2 \end{bmatrix} \begin{bmatrix} \eta^1 \\ \eta^2 \end{bmatrix} &= \begin{bmatrix} \mathbf{f}_c^1 + \mathbf{f}_{\text{PTO}} \\ \mathbf{f}_c^2 - \mathbf{f}_{\text{PTO}} \end{bmatrix} \\ \begin{bmatrix} \dot{\mathbf{u}}^1 \\ \dot{\mathbf{u}}^{12} \\ \dot{\mathbf{u}}^2 \\ \dot{\mathbf{u}}^{21} \end{bmatrix} &= \begin{bmatrix} \mathbf{A}_r^1 & \mathbf{0} & \dots & \mathbf{0} \\ \mathbf{0} & \mathbf{A}_r^{12} & \mathbf{0} & \vdots \\ \vdots & \mathbf{0} & \mathbf{A}_r^2 & \mathbf{0} \\ \mathbf{0} & \dots & \mathbf{0} & \mathbf{A}_r^{21} \end{bmatrix} \begin{bmatrix} \mathbf{u}^1 \\ \mathbf{u}^{12} \\ \mathbf{u}^2 \\ \mathbf{u}^{21} \end{bmatrix} + \begin{bmatrix} \mathbf{B}_r^1 & \mathbf{0} \\ \mathbf{0} & \mathbf{B}_r^{12} \\ \mathbf{0} & \mathbf{B}_r^2 \\ \mathbf{B}_r^{21} & \mathbf{0} \end{bmatrix} \begin{bmatrix} \dot{\eta}^1 \\ \dot{\eta}^2 \end{bmatrix} \end{aligned} \quad (9)$$

damping $\lambda(\omega)$ in the frequency domain

$$\mathbf{h}_r(t) = \frac{2}{\pi} \int_0^\infty \omega(\mathbf{m} - \mu(\omega)) \sin(\omega t) d\omega = \frac{2}{\pi} \int_0^\infty \lambda(\omega) \cos(\omega t) d\omega \quad (6)$$

The transfer function from the velocity $\dot{\eta}(t)$ to the radiation force $\mathbf{f}^R(t)$ can be approximated with polynomial equations, and represented in state-space form

$$\begin{aligned} \mathbf{f}^R(t) &= \mathbf{C}_r \mathbf{u}(t) \\ \dot{\mathbf{u}}(t) &= \mathbf{A}_r \mathbf{u}(t) + \mathbf{B}_r \dot{\eta}(t) \end{aligned} \quad (7)$$

The system matrices \mathbf{A}_r , \mathbf{B}_r and \mathbf{C}_r are derived by frequency-domain identification (FDI) using the MSS FDI toolbox (Perez and Fossen, 2009); $\mathbf{u}(t)$ is an intermediate vector representing the state of the system. Hence, with the state-space representation of radiation term in Eq. (7), Eq. (1) can be written as

$$\begin{aligned} (\mathbf{M} + \mathbf{m}) \ddot{\eta}(t) + \mathbf{C}_r \mathbf{u}(t) + \mathbf{K} \eta(t) &= \mathbf{f}_c(t) + \mathbf{f}_{\text{PTO}}(t) \\ \ddot{\mathbf{u}}(t) &= \mathbf{A}_r \mathbf{u}(t) + \mathbf{B}_r \dot{\eta}(t) \end{aligned} \quad (8)$$

Equation (8) can also be written in a matrix form as

The superscript 12 represents the coupled interaction of *Box_1* to *Box_2*, and vice versa.

2.3. Constraint matrix of a *N*-body hinged system

The discussion is initiated from a two-box system. Because of the constraints at the hinge point, there are no relative motions in the surge, sway, heave, roll, and yaw directions at the hinge point. Hinge constrains the motions at the hinge point of the two bodies to be the same, except for the pitch direction. As illustrated in Fig. 2, the relative angle

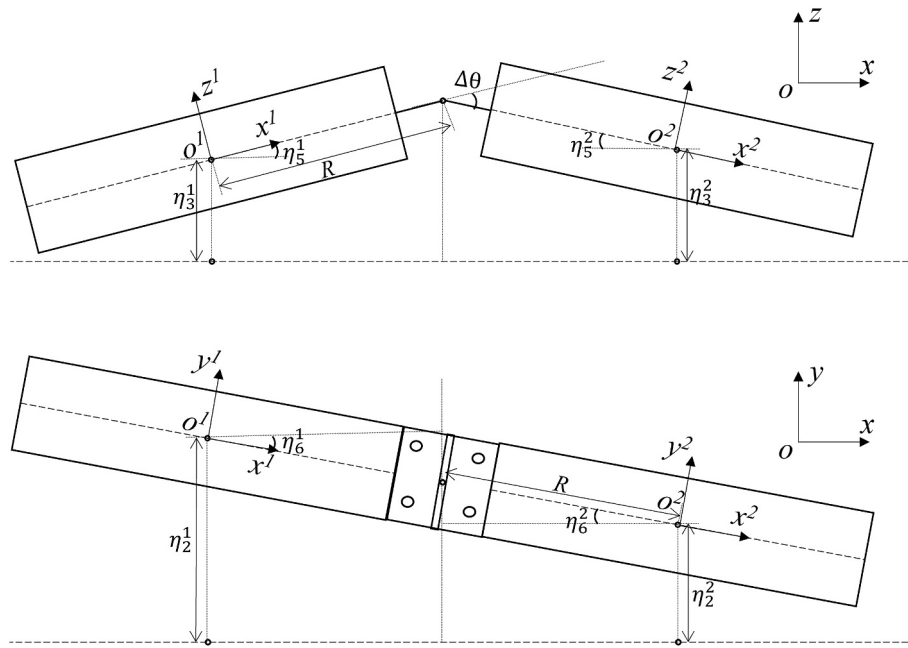


Fig. 2. Relationship of motions in front view (upper) and top view (below) of the two-box system.

$\Delta\theta$ at the hinge point of the two bodies can be calculated from the difference between their respective pitch angles in the body-fixed coordinate. Thus, the constraint equations are as follows.

$$\left\{ \begin{array}{l} \eta_1^1 = \eta_1^2 \\ \eta_2^1 + R \sin \eta_6^1 = \eta_2^2 - R \sin \eta_6^2 \\ \eta_3^1 - R \sin \eta_5^1 = \eta_3^2 + R \sin \eta_5^2 \\ \eta_4^1 = \eta_4^2 \\ \eta_5^1 = \eta_5^2 - \Delta\theta \\ \eta_6^1 = \eta_6^2 \end{array} \right. \quad (10)$$

in which R is the value of distances from the CoGs of the bodies to the hinge point. According to Airy wave theory (Airy, 1845), the pitch amplitude follows the small-angle approximation, so $\sin \eta_5$ and $\sin \eta_6$ can be written as η_5 and η_6 . The constraint equation set can be linearised to Eq. (11). It can be written in matrix form as Eq. (12).

$$\left\{ \begin{array}{l} \eta_1^1 = \eta_1^2 \\ \eta_2^1 + R\eta_6^1 = \eta_2^2 - R\eta_6^2 \\ \eta_3^1 - R\eta_5^1 = \eta_3^2 + R\eta_5^2 \\ \eta_4^1 = \eta_4^2 \\ \eta_5^1 = \eta_5^2 - \Delta\theta \\ \eta_6^1 = \eta_6^2 \end{array} \right. \quad (11)$$

$$\eta^2 = \begin{bmatrix} \eta_1^2 \\ \eta_2^2 \\ \eta_3^2 \\ \eta_4^2 \\ \eta_5^2 \\ \eta_6^2 \end{bmatrix} = \begin{bmatrix} 1 & 0 & 0 & 0 & 0 & 0 \\ 0 & 1 & 0 & 0 & 0 & 2R \\ 0 & 0 & 1 & 0 & -2R & 0 \\ 0 & 0 & 0 & 1 & 0 & 0 \\ 0 & 0 & 0 & 0 & 1 & 0 \\ 0 & 0 & 0 & 0 & 0 & 1 \end{bmatrix} \begin{bmatrix} \eta_1^1 \\ \eta_2^1 \\ \eta_3^1 \\ \eta_4^1 \\ \eta_5^1 \\ \eta_6^1 \end{bmatrix} + \begin{bmatrix} 0 \\ 0 \\ -R \\ 0 \\ 1 \\ 0 \end{bmatrix} [\theta] \quad (12)$$

$$= S_{21}\eta^1 + S_{22}\theta$$

which indicates that the motions of *Box_2* can be represented by the motions of *Box_1* and the relative angle $\Delta\theta$. The motion matrix of the system can be rewritten as

$$\eta = \begin{bmatrix} \eta^1 \\ \eta^2 \end{bmatrix} = \begin{bmatrix} I & \mathbf{0} \\ S_{21} & S_{22} \end{bmatrix} \begin{bmatrix} \eta^1 \\ \theta \end{bmatrix} = S \begin{bmatrix} \eta^1 \\ \theta \end{bmatrix} = S\eta' \quad (13)$$

S is the coefficient matrix of hinge constraints; I is an identity matrix. In the motion equation of the system, η^2 , $\dot{\eta}^2$, $\ddot{\eta}^2$ can be replaced by η^1 , $\dot{\eta}^1$, $\ddot{\eta}^1$ and $\Delta\theta$, $\dot{\Delta\theta}$, $\ddot{\Delta\theta}$. Substituting η with η' , the original 12-DoF Eq. (8) can be transformed into a 7-DoF equation as following

$$\begin{aligned} S^T(M + m)\ddot{\eta}'(t) + S^T C_r u(t) + S^T K S \eta'(t) &= S^T f_e(t) + S^T f_{PTO}(t) + S^T f_h(t) \\ \ddot{u}(t) &= A_r u(t) + B_r S \eta'(t) \end{aligned} \quad (14)$$

The hinge forces f_h can be eliminated when it multiplies the matrix S^T , because in the coordinate system of the hinge system, the hinge forces are internal forces. According to Newton's third law, the hinge forces and torques of *Box_1* and *Box_2* are of equal magnitude and opposite direction, for example $f_{h,1}^1 = -f_{h,1}^2$. The torques need to be superimposed with the product of relevant forces and arms, for example $f_{h,5}^1 = -Rf_{h,3}^1$. The mathematical derivation can be seen as following

$$S^T f_h(t) = S^T \begin{bmatrix} f_{h,1}^1 \\ f_{h,2}^1 \\ f_{h,3}^1 \\ f_{h,4}^1 \\ -Rf_{h,3}^1 \\ f_{h,6}^1 + Rf_{h,2}^1 \\ f_{h,1}^2 \\ f_{h,2}^2 \\ f_{h,3}^2 \\ f_{h,4}^2 \\ Rf_{h,3}^2 \\ f_{h,6}^2 - Rf_{h,2}^2 \end{bmatrix} = \begin{bmatrix} f_{h,1}^1 \\ f_{h,2}^1 \\ f_{h,3}^1 \\ f_{h,4}^1 \\ f_{h,6}^1 + f_{h,1}^2 \\ f_{h,2}^1 + f_{h,2}^2 \\ f_{h,3}^1 + f_{h,3}^2 \\ f_{h,4}^1 + f_{h,4}^2 \\ -Rf_{h,3}^1 - 2Rf_{h,3}^2 + f_{h,5}^2 \\ f_{h,6}^1 + Rf_{h,2}^1 + 2Rf_{h,2}^2 + f_{h,6}^2 - Rf_{h,2}^2 \\ -Rf_{h,3}^2 + Rf_{h,3}^2 \end{bmatrix} = \mathbf{0} \quad (15)$$

For an N -body system, there is one hinge connection between each pair of adjacent bodies. The total constraint matrix is the product of the individual constraint matrices. The motion matrix of the system can be rewritten as

$$\eta = \begin{bmatrix} \eta^1 \\ \eta^2 \\ \vdots \\ \eta^{N-1} \\ \eta^N \end{bmatrix} = \begin{bmatrix} I & \mathbf{0} & \cdots & \mathbf{0} & \mathbf{0} \\ S_{21} & S_{22} & \cdots & \mathbf{0} & \mathbf{0} \\ \vdots & \vdots & \ddots & \vdots & \vdots \\ S_{21}^{N-2} & S_{21}^{N-3} S_{22} & \cdots & S_{22} & \mathbf{0} \\ S_{21}^{N-1} & S_{21}^{N-2} S_{22} & \cdots & S_{21} S_{22} & S_{22} \end{bmatrix} \begin{bmatrix} \eta^1 \\ \Delta\theta^1 \\ \vdots \\ \Delta\theta^{N-2} \\ \Delta\theta^{N-1} \end{bmatrix} \quad (16)$$

$$= S \begin{bmatrix} \eta^1 \\ \Delta\theta^1 \\ \vdots \\ \Delta\theta^{N-2} \\ \Delta\theta^{N-1} \end{bmatrix} = S\eta'$$

3. Control theory

3.1. Declutching control

When the control command of declutching control is 0, the value of damping force is $B_{PTO}\Delta\dot{\theta}$; when the control command is 1, the damping force is 0. The range of PTO damping in the latching control varies from a constant value to infinite; for declutching control, the range is from 0 to a constant value.

When the binary control command, β , is introduced to Eq. (14), the controlled PTO forces can be written as

$$f_{PTO} = -(B_{PTO} + \beta(t)B_c)\Delta\dot{\theta}(t) \quad (17)$$

where B_c and B_{PTO} represent the damping coefficients of the control device and the PTO system in pitch direction. We define that $B_c = -B_{PTO}$ in declutching control, representing the PTO is switched off when declutching control is activated. Define the total declutching control damping coefficient as $B_d(t) = B_{PTO} + \beta(t)B_c$. An example of the time history of B_d is shown in Fig. 3. In the following discussions, “without control” refers to not considering declutching control, but with damping control; whereas “with control” indicates that the PTO damping is not a constant but a discrete variable (referring to Eq. (17)) that can be controlled to optimise the system’s performance (see Fig. 4).

Define the state vector $x = [\eta'(t), \dot{\eta}'(t), u(t)]^T$, Eq. (14) can be written in state-space representation as

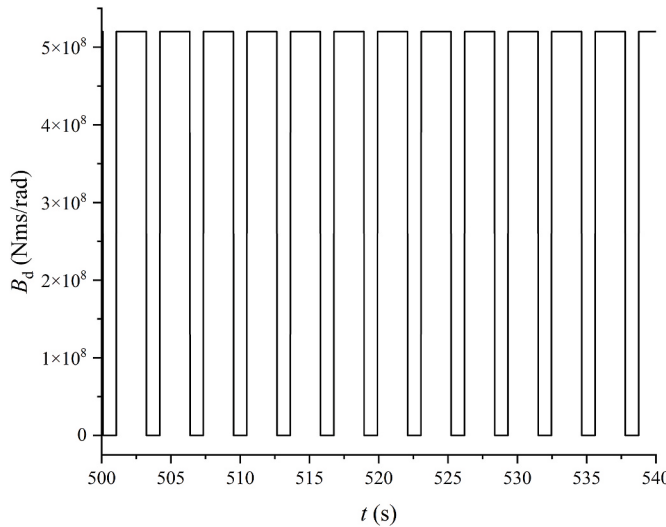


Fig. 3. Time history of the total damping coefficient under declutching control.

$$\dot{x} = \gamma \bullet x + \varepsilon$$

$$\gamma = \begin{bmatrix} \mathbf{0} & \Lambda & \mathbf{0} \\ \frac{S^T K S}{S^T M S} & \frac{S^T (B S + B_{PTO} + \beta(t) B_c)}{S^T M S} & \frac{S^T C_r}{S^T M S} \\ \mathbf{0} & B_r S & A_r \end{bmatrix},$$

$$\varepsilon = \begin{bmatrix} \mathbf{0} \\ -\frac{f_c(t)}{S^T M S} \\ \mathbf{0} \end{bmatrix} \quad (18)$$

This linearised expression is more convenient for computation and adding a damping force as the control force. Furthermore, the hydrodynamic interactions between multiple bodies induced by wave radiation are also considered.

3.2. Pontryagin's maximum principle

Pontryagin's maximum principle (PMP) is a powerful tool in optimal control theory that is widely used to find the optimal control inputs that minimise or maximise objective functions. Objective functions represent the objectives that are being optimised. In this research, PMP is employed to solve the control commands that result in a minimum motion of floating bodies or a maximum power absorption of PTO devices over a given computation period. These objective functions are computed along the trajectory of the system, which describes the system's motion from its initial static state to its final state.

In order to minimise or maximise the target objective function, we need to minimise or maximise the Hamiltonian, H , calculated by the state of the system.

$$H = L + \lambda(\gamma \bullet x + \varepsilon)$$

$$\dot{\lambda} = -\frac{\partial H}{\partial x} = -\frac{\partial L}{\partial x} - \lambda\gamma \quad (19)$$

where λ is the Lagrange multiplier and L is the Lagrangian function, i.e., the performance index. By solving the value of λ , the Hamiltonian H containing $\beta(t)$ can be derived. There are two unknown variables in the dynamic equation and Pontryagin's equation: the system state x and the control command β . In theory, Eqs. (18) and (19) can be coupled and solved together. However, since the dynamic equation is a 2nd ordinary differential equation, we choose to linearise the system and solve the system state x with a numerical method in Matlab before substituting it

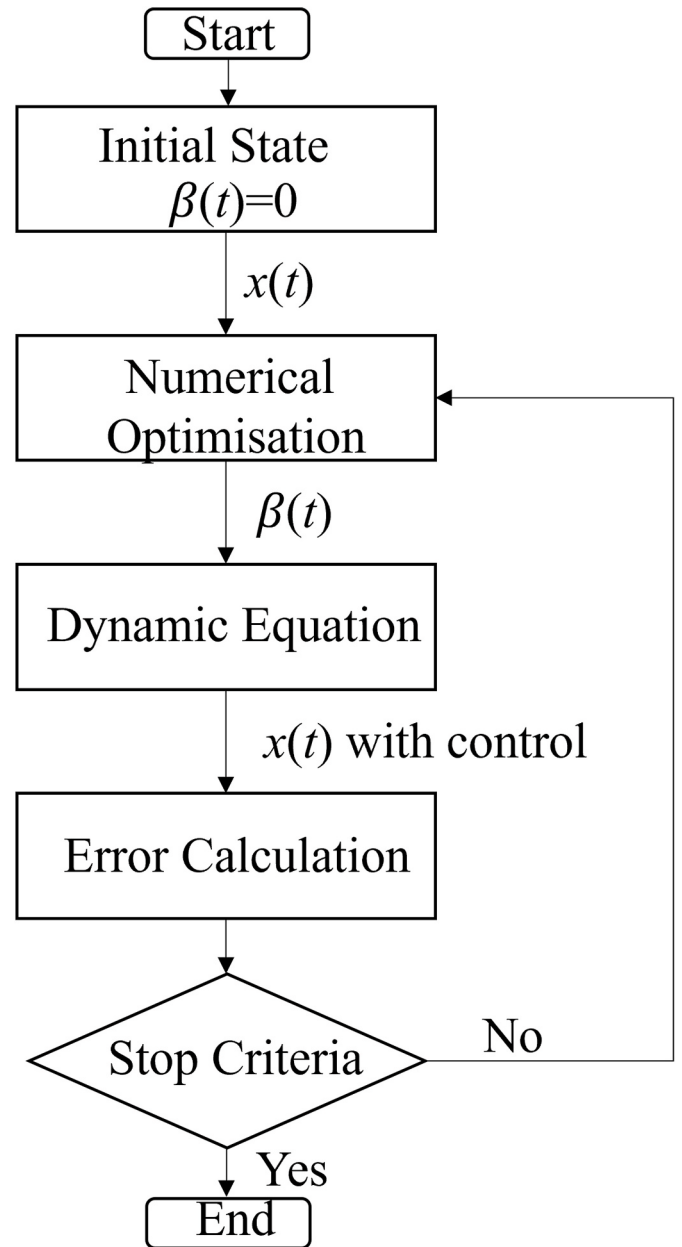


Fig. 4. Flow chart of optimal declutching control process.

into the equation of Pontryagin's theorem. In discrete control, the control command $\beta(t)$ is binary, which means the command is either 0 or 1. If H needs to be maximised, β is defined as

$$\beta = \begin{cases} 0, \lambda^T (8 : 14) \frac{S^T [-B_c; B_c] \dot{\theta}}{S^T M S} < 0 \\ 1, \text{otherwise} \end{cases} \quad (20)$$

If H needs to be minimised, β is defined as

$$\beta = \begin{cases} 1, \lambda^T (8 : 14) \frac{S^T [-B_c; B_c] \dot{\theta}}{S^T M S} < 0 \\ 0, \text{otherwise} \end{cases} \quad (21)$$

The key point is to extract the term that includes the control command β from Eq. (19). To maximise the objective function, the strategy is: if the term is greater than 0, set $\beta = 1$ and retain the term; conversely, if the term is less than 0, set $\beta = 0$ and don't count the term. When the

goal is to minimise the objective function, the opposite strategy is applied. After β is solved, the responses with control can be computed. The responses with control are introduced to the iteration as the initial state until the control command converges and reaches its numerical optimum.

The controller developed in this research is not designed as a real-time controller, as it does not incorporate the prediction of future information. However, it can be regarded as the optimisation part of Model Predictive Control (MPC), which contains three subsections: prediction, optimisation, and control.

3.3. Objective function

The objective function J is defined as a physical value that is optimised during the numerical optimisation process in the time interval $[T_1, T_2]$, representing the performance of the system in a period $T_2 - T_1$.

$$J = \frac{1}{T_2 - T_1} \int_{T_1}^{T_2} L dt \quad (22)$$

J reaches its maximum or minimum when H is maximised or minimised. As there are no constraints at the final state in this paper's cases, each objective function only includes the time-average value of the Lagrangian function. To serve different objectives in varying optimisation scenarios, several alternative objective functions are investigated, which are expressed by

$$J_1 = |\dot{\eta}_5^1| = \frac{1}{T_2 - T_1} \int_{T_1}^{T_2} |\dot{\eta}_5^1(t)| dt \quad (23)$$

$$J_2 = P_{\text{wave}} = \frac{1}{T_2 - T_1} \int_{T_1}^{T_2} \left\{ f_{e,5}^1(t) \dot{\eta}_5^1(t) + f_{e,5}^2(t) \dot{\eta}_5^2(t) \right\} dt \quad (24)$$

$$J_3 = |\Delta\dot{\theta}| = \frac{1}{T_2 - T_1} \int_{T_1}^{T_2} |\Delta\dot{\theta}(t)| dt \quad (25)$$

$$J_4 = P_{\text{PTO}} = \frac{1}{T_2 - T_1} \int_{T_1}^{T_2} B_d(t) \Delta\dot{\theta}(t)^2 dt \quad (26)$$

When J_1 is applied, the physical meaning is that the average pitch speed of *Box_1* is minimised. This corresponds to a scenario of stabilising platforms or substructures of floating wind turbines or photovoltaics in various wave conditions. When J_2 is applied, the total power of wave force, $f_{e,5}\dot{\eta}_5$, is maximised. It corresponds to a scenario of increasing the conversion from wave energy to kinetic energy of multiple floating bodies and providing a shielded area with fewer waves to protect other floating facilities. When J_3 is applied, the average relative angular speed of rotation between the two boxes is maximised. Currently, there is no application in ocean engineering that focuses on directly realising this objective. When J_4 is applied, the physical meaning is that the energy absorption of PTO is maximised. It corresponds to a scenario of increasing the power output of WECs which harness relative pitch motion between sections. The selection of the objective function depends on the optimisation goal.

4. Results and discussion

This section presents an analysis of a typical hinged-box system, as shown in Fig. 2. The hydrodynamic results, including the hydrodynamic coefficients and wave excitation forces, are obtained by using a 3D potential flow solver MHydro that has been developed and validated at the University of Strathclyde (Yuan et al., 2015; Zhang et al., 2022). To ensure the motion responses in regular waves converge, the total computation time in MATLAB is set to be 1000 s and the steady motions between 500 and 540 s are presented. In this study, it is assumed that wave excitation forces are already known in all time horizons.

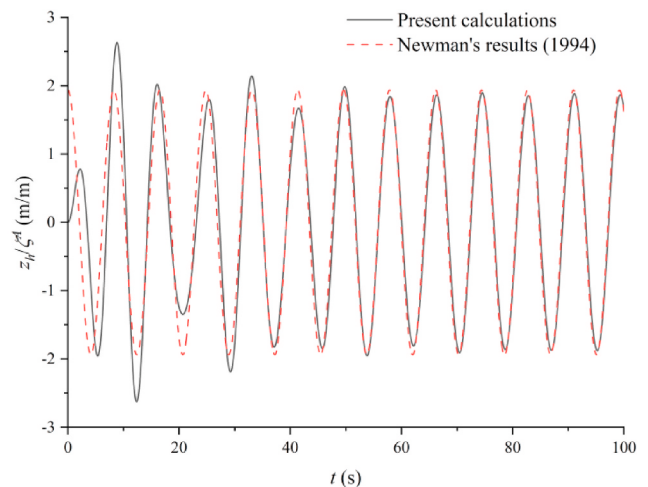
4.1. Model validation

This section validates the established hinged multiple floating bodies model with the results of hinged boxes in Neman's research (Newman, 1994). The responses for heave and hinge deflection when the wave frequency is specified as 0.76 rad/s are computed in the time domain.

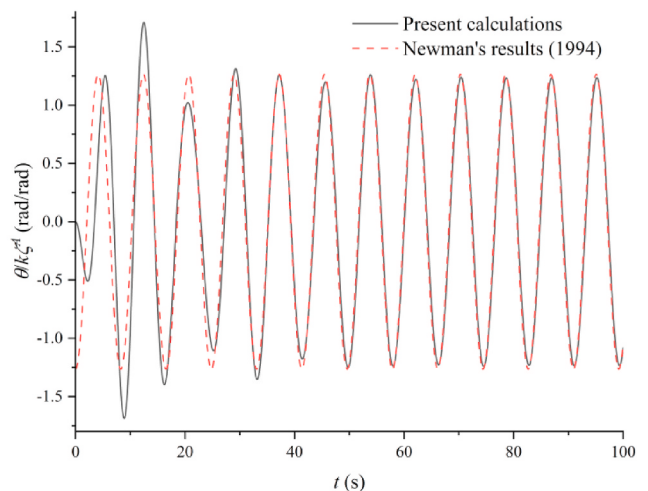
The result in Newman's research at a wave frequency of 0.76 rad/s is transformed into the time domain using Fourier transformation. Fig. 5 shows a comparison of the results of the present study and Newman's research, showing good agreement after convergence. Due to the damping effect with time, the initial condition of the system will eventually become negligible and thus have no significant influence on the system's response. It confirms the validity of the present method, which solves the time-domain motion equation of hinged bodies with a constraint matrix.

4.2. Number of iterations

To determine when the numerical optimisation reaches convergence, stop criteria are established for the selected performance indices. These stop criteria include a critical number of iterations and a critical error.



(a) The time series for normalised heave motion at hinge point.



(b) The time series for normalised angular deflection at hinge point.

Fig. 5. The time series for normalised heave motion and angular deflection at hinge point.

The iteration of the control algorithm is stopped when $n = N_{\text{critical}}$ or $\text{err} < \text{err}_{\text{critical}}$ where n is the number of the current iteration, N_{critical} is the critical number of iterations, err is the error of performance index and $\text{err}_{\text{critical}}$ is the critical error.

The error of the performance index is expressed as follows

$$\text{err} = \frac{\text{std}(J(n-4:n))}{J(n)} \times 100\% \quad (27)$$

where J is the performance index; $\text{std}(J(n-4:n))$ represents the Standard Deviation (STD) of the performance index in the latest five iterations. Once the STD is lower than the critical value, the index is considered to have reached its convergence, and the computation exits the iteration loop. The critical value is set as 1% of the last performance index in the loop in this paper, namely $\text{err}_{\text{critical}} = 0.01$. Furthermore, when the number of iterations reaches $N_{\text{critical}} = 100$, the iteration also jumps to the end. Fig. 6 shows the logarithmic scale of err under different objective functions when the wave amplitude is 1 m and the wave frequency is 1 rad/s.

In Fig. 6, the err of each objective function decreases over time and eventually reaches below the critical value $\text{err}_{\text{critical}} = 0.01$. The err reaches the critical value at different iteration steps, which means the convergence speed of the objective functions varies depending on the objective function selection. J_1 , J_2 , and J_3 converge quickly and steadily, while J_4 have slower and more fluctuating convergence. This indicates that the numerical optimisation process for J_4 requires more iterations to reach convergence compared to other objective functions.

When the objective functions converge quickly, the objective function is typically in a relatively simple form and can be easily optimised, referring to J_1 , J_2 , and J_3 . In these cases, the convergence is relatively fast, and the objective function can be considered to have reached a local optimum. The difference in their err after convergence is related to their function forms. On the other hand, when the objective functions converge slowly, such as J_4 , the reason is that it is more sensitive to the PTO control strategy, which introduces more complexity to the numerical optimisation process. According to Eq. (26), the objective function of J_4 contains multiple time-variant variables, $B_d(t)$ and $\Delta\dot{\theta}(t)$. The time-variant variables vary with each iteration, so the objective functions are optimised along a different trajectory in each iteration, which makes it more difficult to converge. The next section will provide a more detailed analysis of their performance.

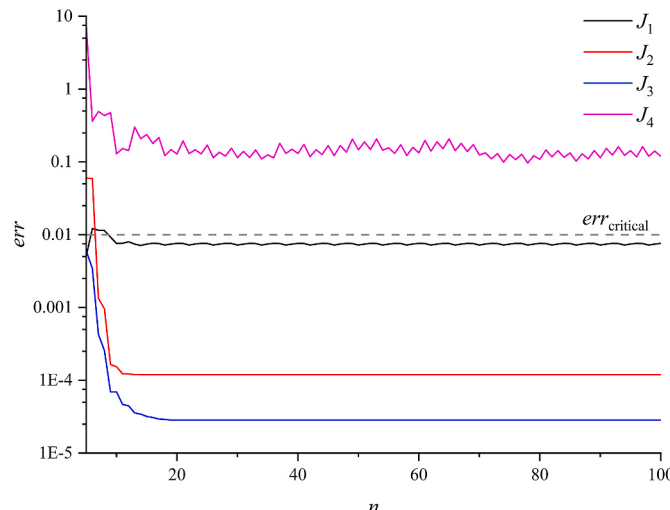


Fig. 6. The convergence of different objective functions with the number of iterations (The err is shown in logarithmic scale).

4.3. Control effect of different objective functions

In this section, the wave amplitude is set to 1 m, and the wave frequency is set to 1 rad/s. B_{PTO} is set to 5.2×10^8 Nms/rad to ensure the initial damping coefficient is sufficiently large to obtain an appropriate average damping coefficient with declutching control. The wave frequency of 1 rad/s is selected to obtain a significant response and control effect under the wave amplitude of 1 m. The time horizon after convergence, 500 s–540 s, is selected to demonstrate the time-domain results. This section focuses exclusively on wave forces (moments) and velocities in the pitch direction, which are affected by the PTO.

Fig. 7 compares the performance of different objective functions in four corresponding objectives. In Fig. 7(a), only J_1 leads to the reduction of $|\dot{\eta}_5^1|$ by 2.94%, while the other three cases result in an increase in $|\dot{\eta}_5^1|$ by more than 539.93%. Therefore, although $|\dot{\eta}_5^1|$ is only minimally optimised, it performs better than other objective functions. In Fig. 7(b) and (c), among the objective functions applied to the control algorithm, J_2 shows the best performance in maximising P_{wave} and J_3 has the best performance in maximising $|\Delta\dot{\theta}|$. This suggests that J_2 is the most effective objective function in maximising P_{wave} , and J_3 is the most effective in maximising $|\Delta\dot{\theta}|$. In Fig. 7(d), P_{PTO} experiences the greatest increase when applying J_4 , but its optimality cannot be guaranteed due to its complexity and slow convergence, as analysed in Section 4.2. In conclusion, each objective function can minimise or maximise its corresponding objective, except J_4 .

In Fig. 7(a), J_2 to J_4 cannot optimise $|\dot{\eta}_5^1|$ to its minimum, indicating that the control effect of J_2 to J_4 contradicts that of J_1 . The control effect of J_2 to J_4 is to maximise their objectives, resulting in the increase of $|\dot{\eta}_5^1|$ as a by-product. The results of J_2 and J_3 are similar in (a), (b) and (c). This implies that J_2 and J_3 have similar effects, i.e., the maximisation of wave power extraction and relative rotational speed have similar conditions. However, the performance of J_2 is 7.76% better than J_3 in (b), while J_3 is 10.01% better than J_2 in (c). This suggests that each performance index can only be optimised when applying its corresponding objective function. The results under other objective functions are suboptimal.

4.3.1. Control effect of J_1

As previously mentioned, J_1 can be slightly optimised under the current conditions. Fig. 8 illustrates that the control command for J_1 is occasionally 1 throughout the simulation, indicating that the declutching control is successfully applied, and the objective $|\dot{\eta}_5^1|$ is reduced. The velocities at the wave frequency of 1 rad/s are shown in Fig. 9. When the velocity of Box_1 is larger than that of Box_2 , Box_2 provides a damping effect on Box_1 through the PTO between them. However, when the velocity of Box_1 is smaller than that of Box_2 , Box_2 provides an actuating effect on Box_1 . In essence, the directions of PTO force and Box_1 's velocity determine whether the force serves as a damping or an actuating force. If the directions are opposite, the PTO force provides a damping force. Conversely, if they are the same, the PTO force provides an actuating force. Fig. 10 shows that when without control, the PTO force is not perfectly anti-phase with the velocity of Box_1 . The declutching control tunes the PTO force to be perfectly anti-phase with the velocity of Box_1 , which provides a maximum damping force to Box_1 .

In another special wave frequency of 1.1 rad/s, it is possible to observe a more obvious motion reduction of Box_1 . At this wave frequency, the responses of the two boxes are the same initially, as shown in Fig. 11. The declutching control releases the two boxes, making their velocities to be different from each other. The velocity of Box_1 is decreased while that of Box_2 is increased with control. Fig. 12 shows that there is almost no in-phase horizon between the PTO force and velocity of Box_1 under the current control algorithm. The current control algorithm ensures that the PTO no longer provides actuating force to Box_1 .

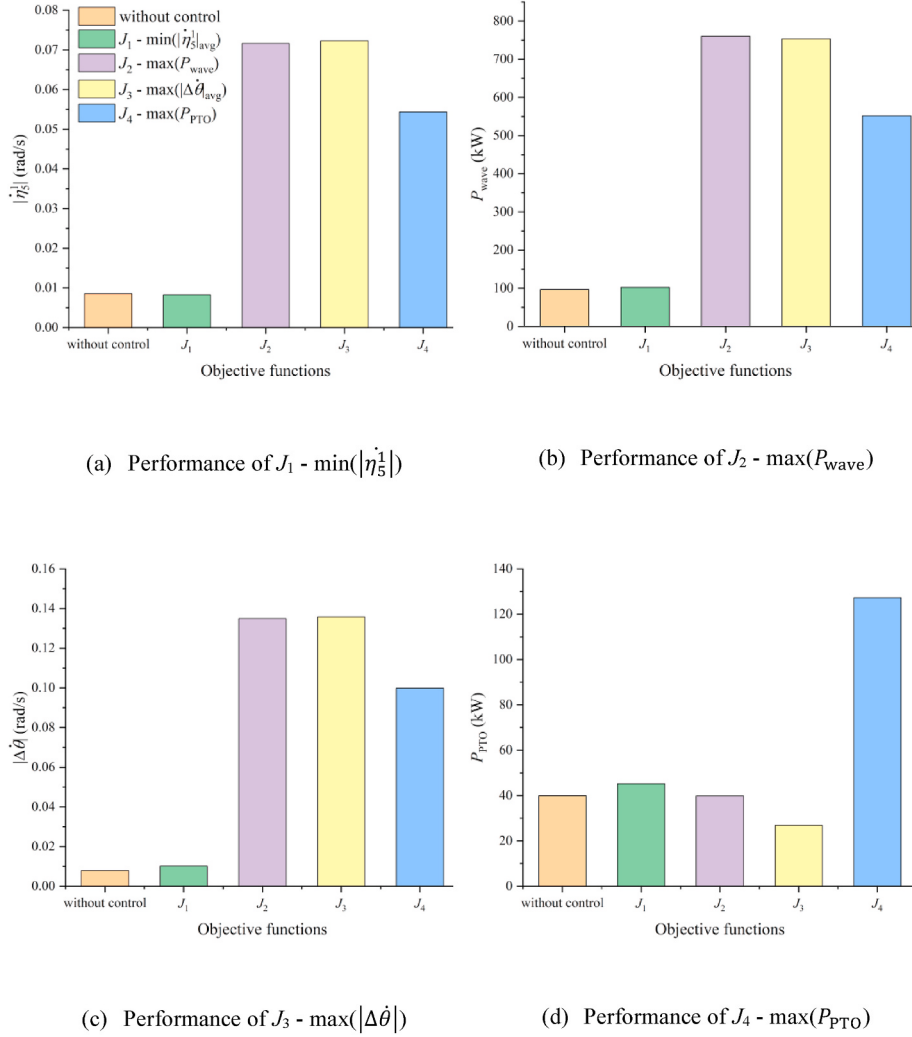


Fig. 7. Performance of J_1 to J_4 when applying different objectives.

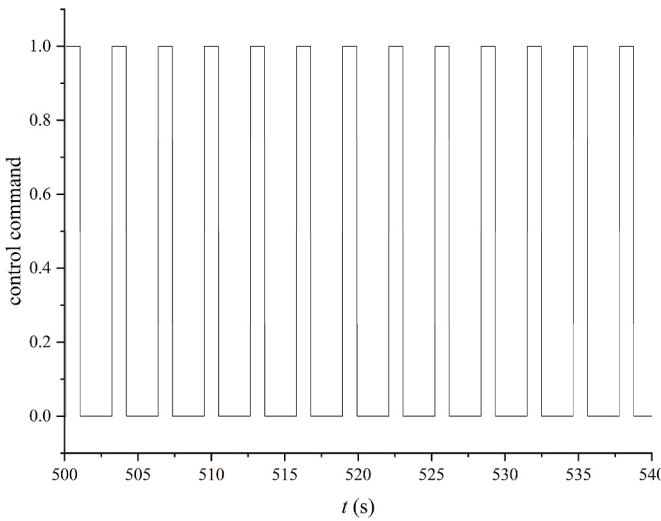


Fig. 8. Control command when applying J_1 as the objective function.

4.3.2. Control effect of J_2

J_2 represents the total power calculated by the product of wave force and body velocity. In most frequencies, the wave force and the body

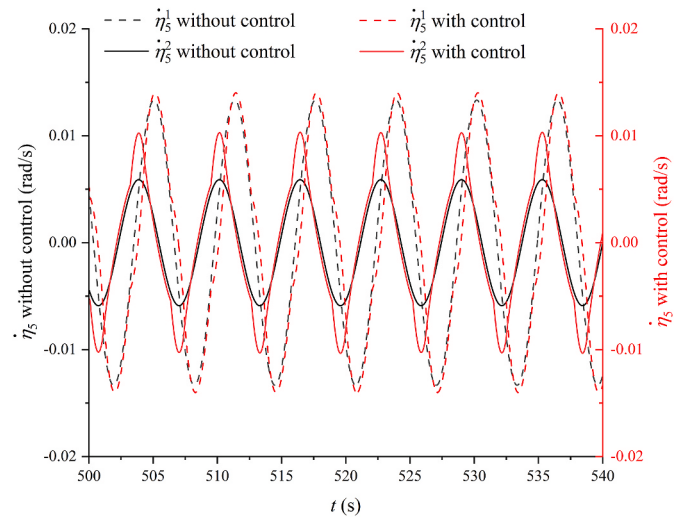


Fig. 9. The time history of the velocities of the two boxes when $\omega = 1$ rad/s.

velocity are not in phase with each other. As a result, each of the boxes extracts and dissipates wave energy in different time horizons. The wave force f_e will not be influenced by the control algorithm, so J_2 is only

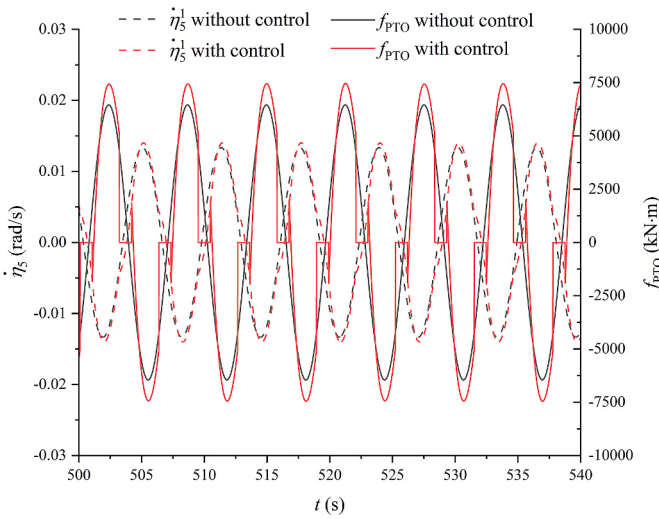


Fig. 10. The relationship of velocity and PTO force of Box_1 when $\omega = 1$ rad/s.

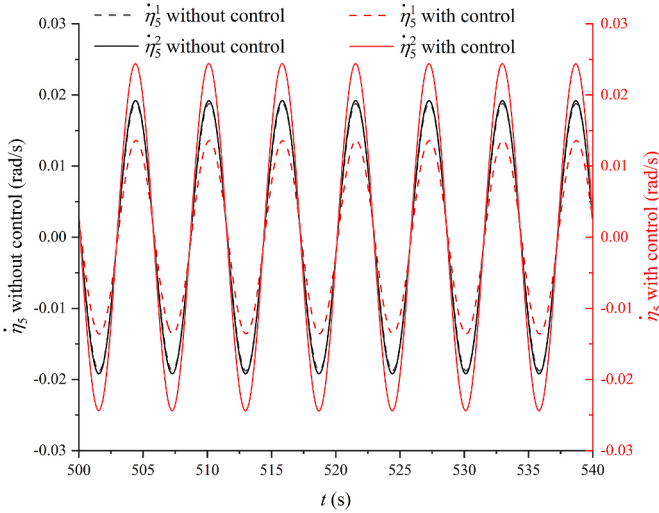


Fig. 11. The phase relationship when $\omega = 1.1$ rad/s under objective function J_1 .

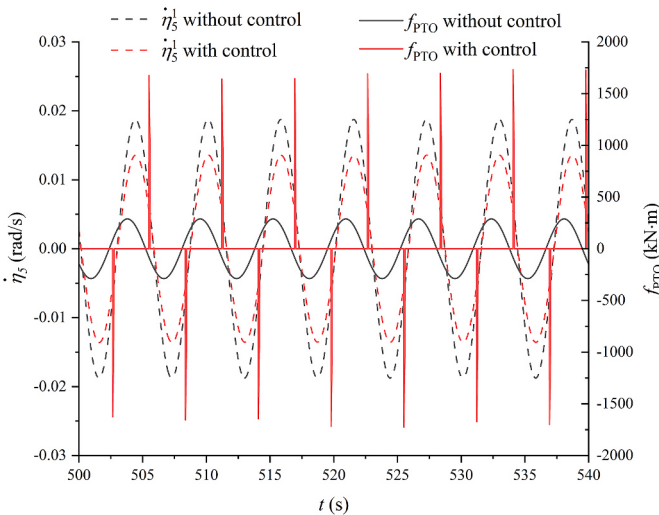
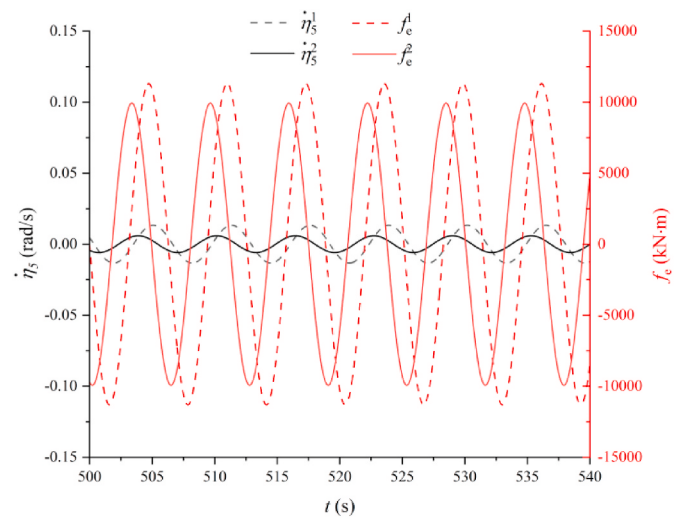


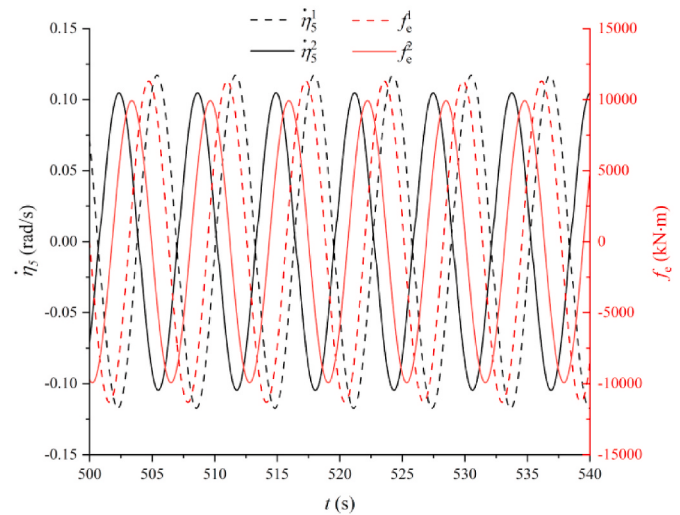
Fig. 12. The relationship of velocity and PTO force of Box_1 when $\omega = 1.1$ rad/s.

influenced by the amplitude of velocities and the phase relationship between the wave force and velocity. The effect of declutching control depends on the weighting between the two factors.

According to Fig. 13, in the case without control, the wave force and velocity of the boxes are not in phase or anti-phase at the current wave frequency. From the energy conservation point of view, in some time horizons, the system absorbs energy from the waves, while in others the system dissipates energy to the environment. At the current wave frequency, the weight of amplitudes of velocities is higher, resulting in a slightly changed force-velocity phase relationship and a noticeable increase in the velocity amplitudes when control is applied. Fig. 14 gives a phase relationship of this trend. The phase relationships in Fig. 14 indicate the boxes have reached steady periodical motions. The areas enclosed between curves and x-axis represent the power of wave forces. In quadrants I and III, the wave forces do positive work to the box, whereas in quadrants II and IV, the wave forces do negative work. With optimal declutching control, the positive power extracted from the waves and the negative power released to the wave are both increased.



(a) Amplitudes of wave force and velocity without control.



(b) Amplitudes of wave force and velocity with control.

Fig. 13. The time-domain results with and without control of the two boxes when J_2 is applied as the objective function.

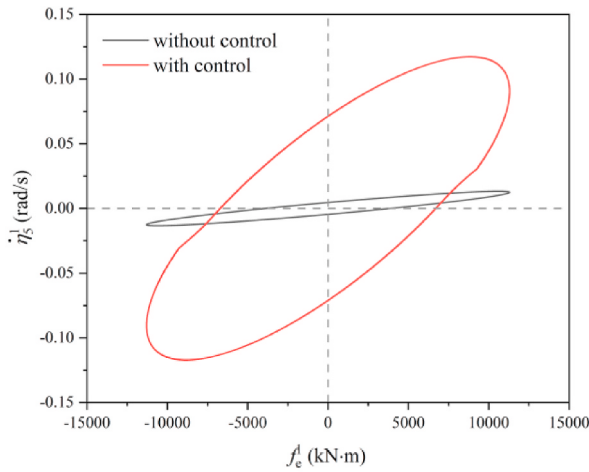
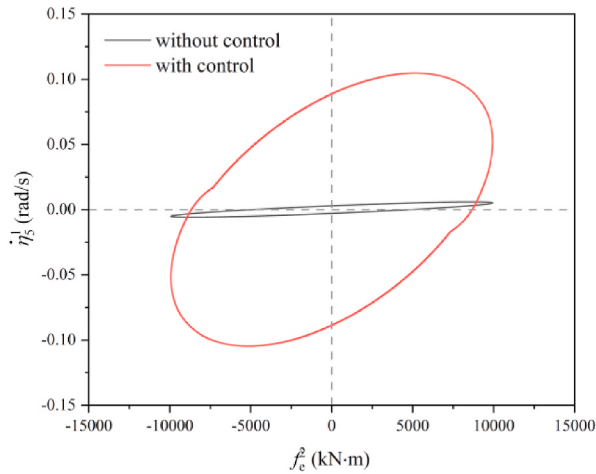
(a) Phase relationship of wave force and velocity of *Box_1*.(b) Phase relationship of wave force and velocity of *Box_2*.

Fig. 14. The phase relationship of wave forces and pitch velocities of the two boxes.

However, the total power increases compared to the case without control. Fig. 15 provides further clarification on the change in extracted wave power. The positions of peak and valley of the wave power extraction in different from those without control. The average wave power is increased by 689.90%, which can also be observed in Fig. 7.

In another special wave frequency 0.8 rad/s, the wave force and velocity of *Box_1* are initially in phase with the current wave frequency, whereas those of *Box_2* are anti-phase (see Fig. 16). The weighting of force-velocity phase is higher at this frequency, so the control effect will be different from above. The wave forces perform positive work on *Box_1* and negative work on *Box_2*. From the energy conservation point of view, *Box_1* keeps absorbing energy from the waves, while *Box_2* keeps dissipating energy to the environment. The optimal declutching control tunes the phase between the wave force and body velocity to maximise J_2 . The in-phase horizon of *Box_2* increases while that of *Box_1* decreases slightly. The amplitudes of velocities are also increased. The phase relationships in Fig. 17 indicate that with optimal declutching control, the positive power extracted from the waves and the negative power released to the wave are both increased. However, the total power increases compared to the case without control. Fig. 18 provides further clarification on the change in extracted wave power. The positive and negative wave power are both increased, and the average wave power is increased.

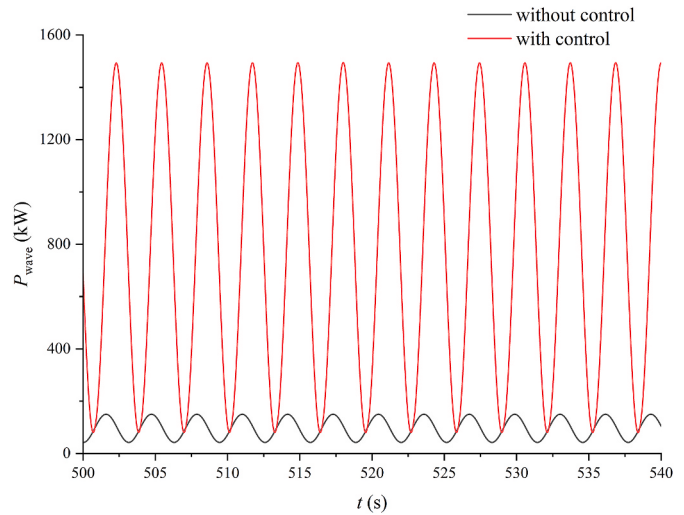


Fig. 15. Total wave power extracted by boxes.

4.3.3. Control effect of J_3

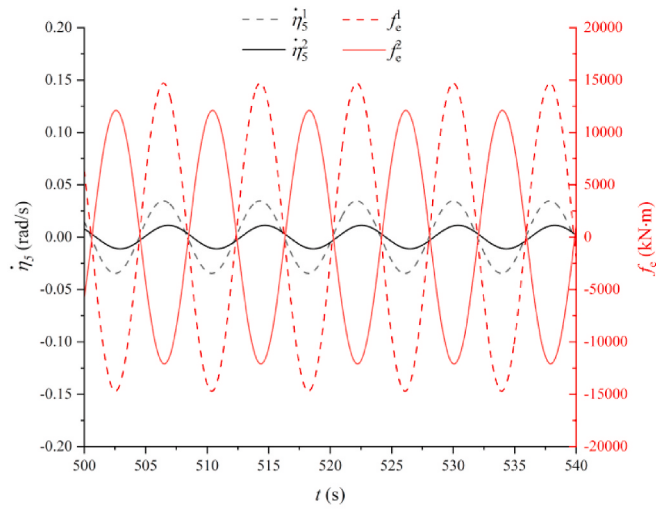
J_3 represents the relative angular velocity between two boxes. Fig. 19 shows that when without control, the average relative angular speed $|\Delta\dot{\theta}|$ is monotonically decreasing with B_{PTO} in regular waves, implying the increase of damping force will cause a reduction in relative motions. It can be anticipated that when B_{PTO} tends to be infinite, the relative angular velocity between the hinged bodies will tend to be 0. Since declutching control can reduce the average value of B_{PTO} , it can effectively maximise $|\Delta\dot{\theta}|$. It should be noted Fig. 19 only depicts the trend of $|\Delta\dot{\theta}|$ and therefore the B_{PTO} used for control in this section, which is 5.2×10^8 Nms/rad, is not included in this figure.

Fig. 20 shows the phase relationship of the velocities of the two boxes and their relationship with the control command. The maximisation of $|\Delta\dot{\theta}|$ depends on the velocity amplitude of each box and the velocities' phase relationship. The velocities initially have a phase difference without control, but with the application of the control strategy, they eventually become anti-phase. When the control command is 1, the optimal declutching control increases the amplitude of the velocities and tunes them anti-phase to maximise $|\Delta\dot{\theta}|$. When the velocities increase in opposite directions, $|\Delta\dot{\theta}|$ also increases, and no control is needed, so the command is 0 during this time period. When both velocities decrease and $|\Delta\dot{\theta}|$ starts to decrease, the control command turns back to 1. The time history of $\Delta\dot{\theta}$ in Fig. 21 demonstrates the amplification effect of the declutching control on the relative angular velocity.

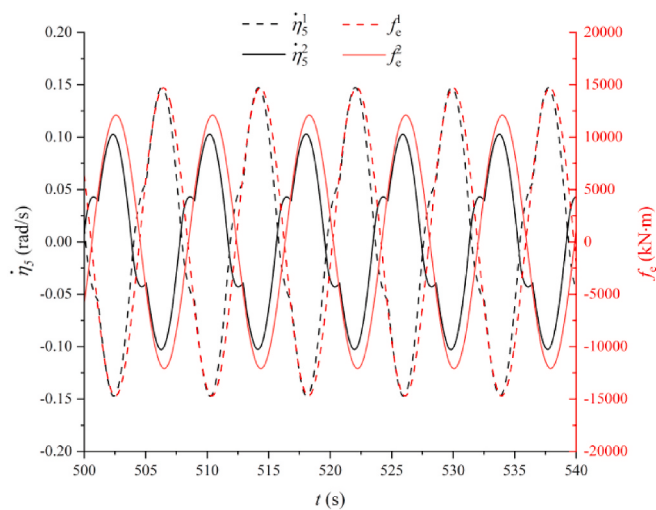
4.3.4. Control effect of J_4

In a single-body system, the velocity of the body is equivalent to the velocity of the PTO, therefore, the in-phase relationship between the body velocity and wave force leads to the maximisation of PTO power output. However, in a multi-body system, the PTO system is installed at the hinge connection between bodies, and the power is generated from the relative motion. Thus, optimising the PTO power output J_4 of a multi-body system is different from optimising wave energy absorption J_2 .

Fig. 22 illustrates the sensitivity of average power to the PTO damping coefficient B_{PTO} in regular waves without control. According to Eq. (3), the average power is determined by B_{PTO} and relative angular velocity $\Delta\dot{\theta}$. The damping coefficient B_{PTO} influence both the velocity $\Delta\dot{\theta}$ and the PTO power output, therefore, the influence of B_{PTO} is nonlinear and noticeable. There is one maximum power absorption at each wave frequency when without control. When B_{PTO} is set to the damping coefficient of 8.5×10^7 Nms/rad and the wave frequency is at 0.84 rad/s, the system reaches its maximum electric power output.



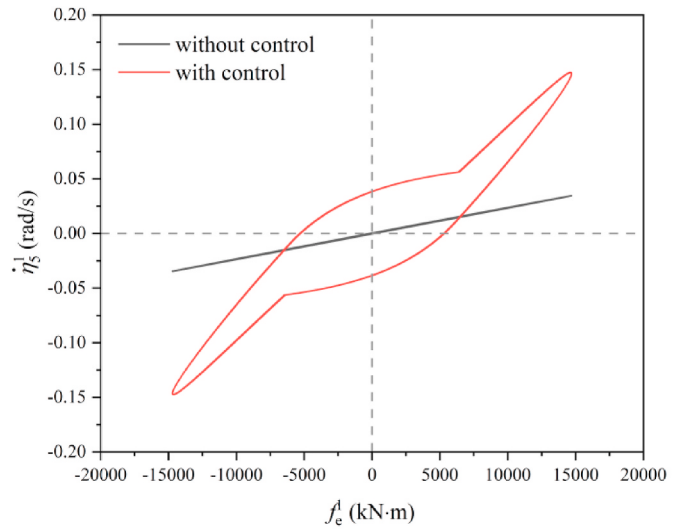
(a) Phase relationship of wave force and velocity without control.



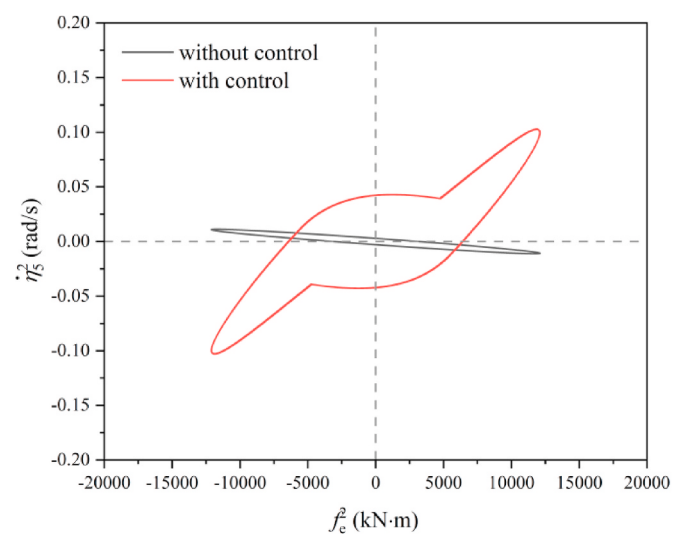
(b) Phase relationship of wave force and velocity with control.

Fig. 16. The time-domain results with and without control of the two boxes when $\omega = 0.8$ rad/s.

Optimal declutching control can realise the effect of tuning dynamically the average damping coefficient to its optimum. Fig. 23 shows the control results when applying J_4 as the objective function. The damping force of PTO under declutching control is $f_d(t) = B_d(t)\Delta\dot{\theta}(t)$. In Fig. 23, $\Delta\dot{\theta}$ varies regularly with f_d . The area under the curves in this plot represents the power of PTO force. However, the horizontal and vertical lines in the plot represent the switch between the binary state of 0 and 1 in declutching control. As the switching time is negligible, these lines can be excluded when computing the power. During the unloading of f_d , $\Delta\dot{\theta}$ increases along vertical line 1. Subsequently, $\Delta\dot{\theta}$ undergoes a sudden decrease along the vertical portion of line 2 as f_d is reloaded. Meanwhile, f_d transiently accelerates to a constant value along the horizontal portion of line 2. While reducing $\Delta\dot{\theta}$, f_d exerts positive power on the PTO system (line 3). Once $\Delta\dot{\theta}$ is too small, f_d is unloaded again (line 4). The lines in quadrant 3 undergo the same process as in quadrant 1. The summation of the positive power is the total power of PTO. The total power of PTO is enhanced with optimal declutching control significantly as shown in Fig. 24. The power output of PTO force under declutching control is



(a) Phase relationship of wave force and velocity of Box_1.



(b) Phase relationship of wave force and velocity of Box_2.

Fig. 17. The phase relationship of wave forces and pitch velocities of the two boxes when $\omega = 0.8$ rad/s.

$P_{\text{PTO}}(t) = f_d(t)\Delta\dot{\theta}(t)$. Although the average time spent producing positive power decreases, both the instantaneous power and the total power generated is higher.

Fig. 25 demonstrates the power distribution in the time horizon of 500 s–544 s, which is approximately 7 wave periods. The results show that the optimal declutching control enhances both the total wave power absorbed by the hinged box system and the power output generated by the system. The summation of power generated by inertial force, radiation force, restoring force, and PTO force is proximate to the total wave power. The proportions of inertial and restoring power are low because kinetic and potential energy does not accumulate over entire periods. Since the radiation force and PTO force are non-conservative, their average power increases with the chosen time horizon. In the current time horizon, the percentage of PTO power increases from 8.86% to 15.68%, indicating that the distribution of wave energy components is beneficial to energy absorption under the optimal declutching control method.

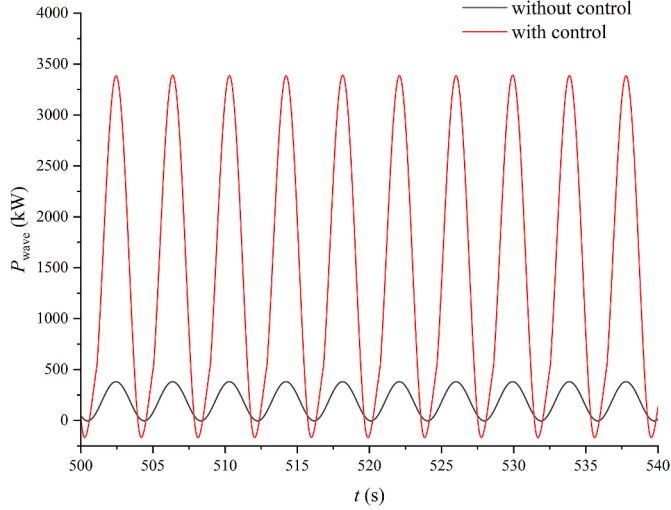


Fig. 18. Total wave power extracted by boxes when $\omega = 0.8 \text{ rad/s}$.

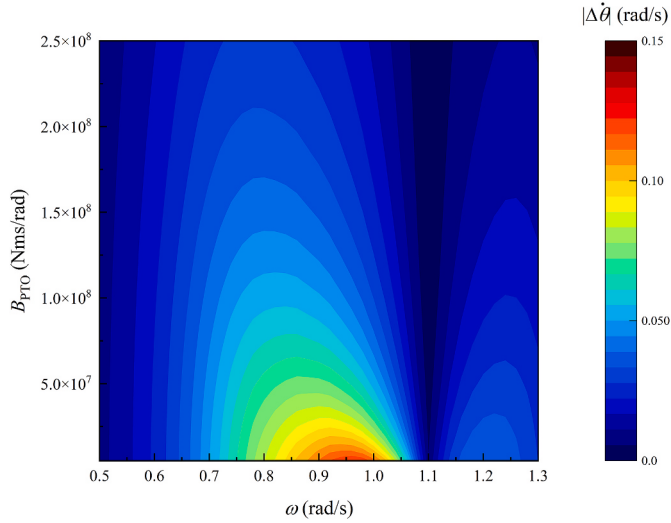


Fig. 19. Average relative angular speed under different PTO damping coefficients and wave frequencies without declutching control.

4.4. Control effect in different wave frequencies

Fig. 26 illustrates the numerical optimisation effects of different performance indices in different wave frequencies. The results are optimised under their respective objective functions.

In general, Fig. 26 shows when the optimal declutching control is applied to the system, all the objectives can be achieved. However, it should be noted that the effect of the control depends on the wave conditions. It indicates that in certain wave frequencies, the control strategy proposed in this study can effectively apply to control the multiple floating bodies with different application scenarios.

In Fig. 26 (a), $|\dot{\eta}_5^1|$ can be optimised at frequencies ranging from 1.0 to 1.15 rad/s. The wavelength in this range is approximately equal to the distance between the CoGs of the boxes, which is 50 m. Therefore, the boxes experience similar wave forces, and their velocities are also similar. As stated in Section 4.3.1, the PTO provides an actuating force to the Box_1 which amplifies Box_1's motion in this condition. The declutching control releases the two boxes and minimises $|\dot{\eta}_5^1|$ by reducing the total force in the direction of its velocity. In other wave frequency ranges, the PTO force acting on Box_1 provides a damping effect most of the time to reduce its motion. Therefore, declutching

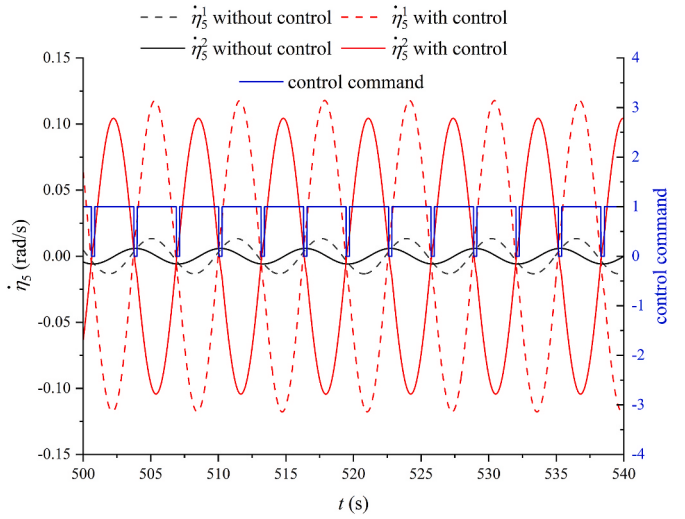


Fig. 20. The time-domain results with and without control of the two boxes when J_3 is applied as the objective function.

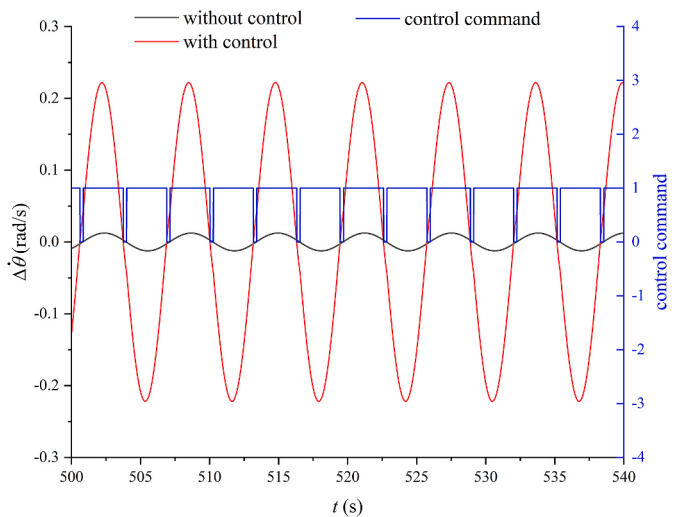


Fig. 21. The time-domain results of the relative angular velocity with and without control. The results are compared with the control command (blue line).

control cannot reduce the pitch speed of Box_1 by releasing the PTO force at these frequencies. In the process of numerical optimisation, the control command for J_1 is 0 nearly throughout the simulation under these wave conditions, indicating that the objective has reached its optimum. In this situation, applying declutching control will increase $|\dot{\eta}_5^1|$.

In Fig. 26(b), P_{wave} can be maximised at most wave frequencies except 1.1–1.25 rad/s. In the frequency range of 1.1–1.25 rad/s, the wave forces of the boxes have similar magnitude, and so do the velocities of the boxes. However, declutching control has a converse effect on the velocity phase of the two boxes. While the phase of Box_1 moves forward, that of Box_2 will move backward and vice versa. They cannot be in phase with their wave force simultaneously. Thus, the convergence in this range will be slow and reach the largest iteration number N_{critical} . The results with control will be not well optimised. In other wave frequencies, there are larger differences in the boxes' velocity amplitudes and phases, so their weightings are different. This leads to a clear numerical optimisation direction and faster convergence.

Fig. 26 (c) shows that $|\Delta\dot{\theta}|$ can be effectively optimised at all wave

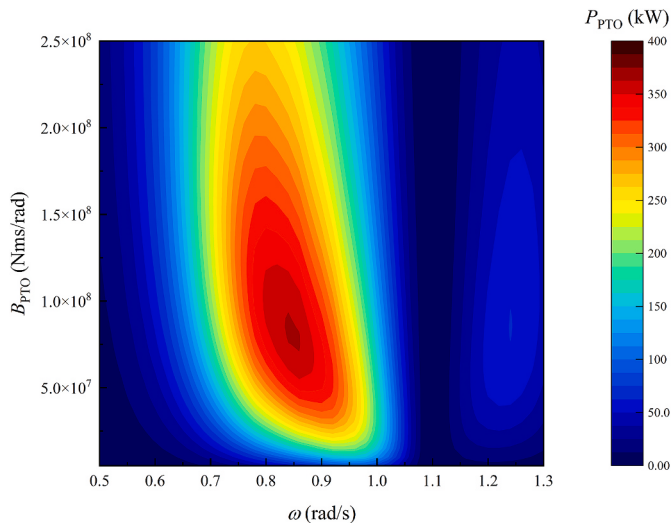


Fig. 22. Power absorption under different PTO damping coefficients and wave frequencies without control.

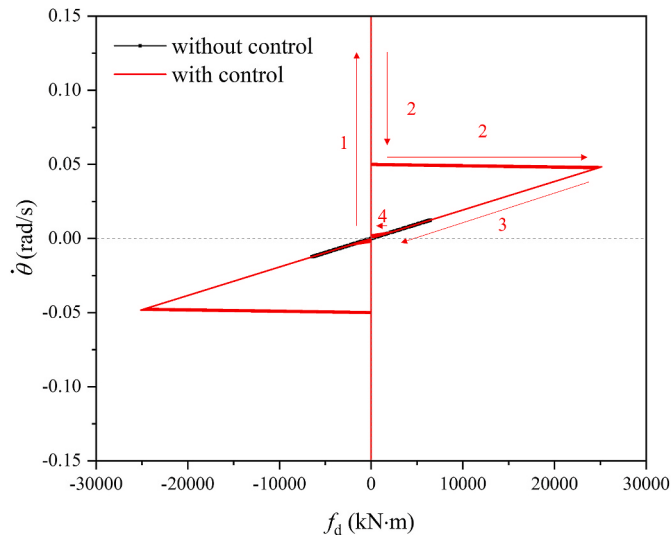


Fig. 23. Phase relationship of the relative angular velocity and the PTO force.

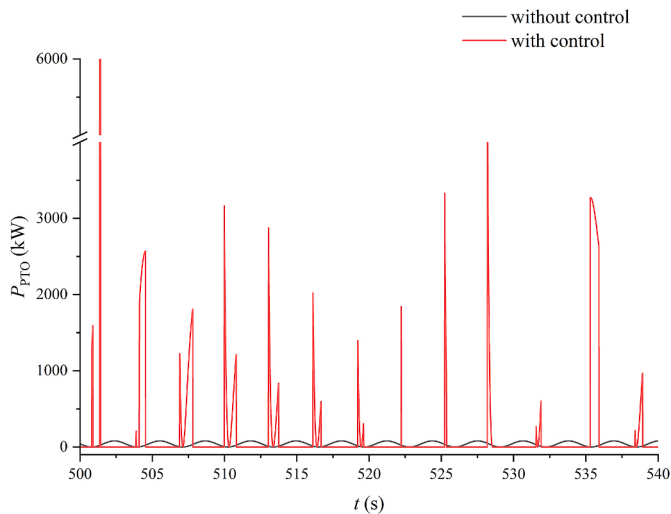


Fig. 24. Time history of the total power absorbed by PTO.

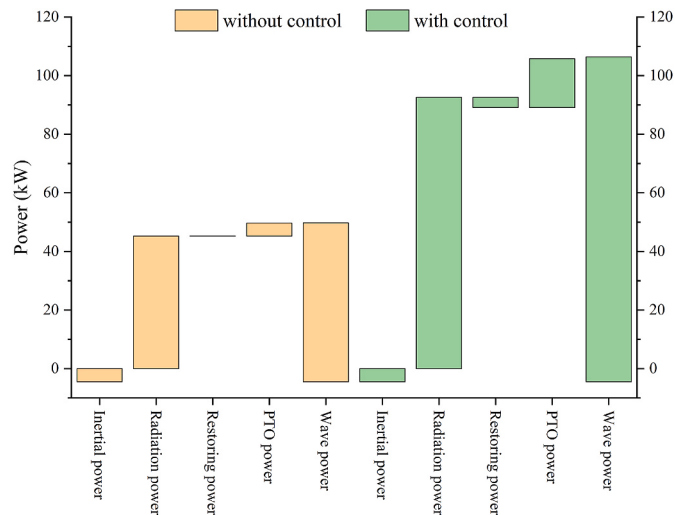


Fig. 25. The distribution of wave energy extracted or dissipated by the hinged box system without (left) and with control (right).

frequencies under J_3 . The optimal declutching control process can tune the average value of $B_d(t)$ to the desired optimal B_{PTO} . According to Fig. 19, the decrease of B_{PTO} will cause an increase in $|\Delta\dot{\theta}|$. The declutching control can reduce the average B_{PTO} at any wave frequency, therefore, optimal declutching control is applicable in all the wave frequencies. When the wave frequency is around 0.8 rad/s, the wavelength (100 m) is approximately twice the distance (50 m) between the CoGs of boxes. Therefore, the boxes experience opposing wave forces, and the directions of their velocities are also opposite. In Fig. 26(c), the best performance can be observed around 0.8 rad/s in the curve without control. The peak of the curve with control is at a different frequency (0.88 rad/s) because the average damping coefficient is lower with control.

Fig. 26 (d) illustrates that the power generation of PTO is improved when J_4 is applied as an objective function of the control system. The improvement covers a wide wave frequency range from 0.6 to 1.1 rad/s. The best control performance is observed at frequencies around 0.8 rad/s, where the P_{PTO} without control is the highest, which is also shown in Fig. 22. The declutching control shortens the oscillation period of the floating body, making it resonant at high-frequency waves. The optimal frequency, at which the best control performance occurs, is determined by the PTO power absorption characteristics of the system. However, as stated in Section 4.2, the objective function of J_4 contains multiple time-variant variables, $B_d(t)$ and $\Delta\dot{\theta}(t)$, therefore, J_4 is difficult to converge under the current optimal control method. The discontinuity and nonlinearity of objective function increase the complexity of this control strategy. Although P_{PTO} is well increased with the objective function J_4 , the result cannot be regarded as optimal.

4.5. Robustness validation in irregular waves

This section discusses the application of the developed control method under irregular wave conditions. The real-world applicability of our model can be demonstrated when tested using irregular waves. Herein, we present the time-domain results of various parameters like velocities, positions, forces, powers, and so on, under irregular waves.

Irregular waves were modelled using a superposition of several regular waves with random phases (Falnes, 2002). The generated wave profile was ensured to statistically represent real sea states by matching with the energy spectrum of standard sea states. Jonswarp wave spectrum is selected to generate irregular waves in this section. The significant wave height H_s is 3.05 m, the peak period T_p is 8.9 s, which are representative conditions for a rough sea state. Take objective function

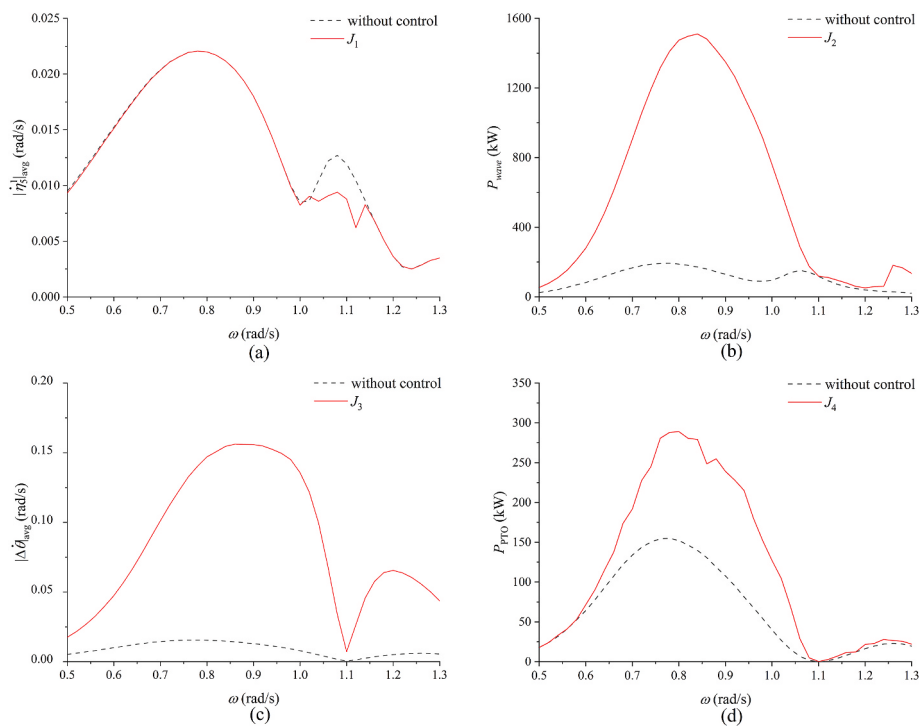


Fig. 26. Performances of different objective functions in different wave frequencies.

J_2 for example, the results $\Delta\dot{\theta}$ and f_{PTO} maintains the relationship of in-phase with our control method, which can be revealed from Fig. 27.

When averaged over time, the results from irregular waves were compared under different objective functions, as shown in Fig. 28. Similar to the control effect in Fig. 7 (d), the energy extracted by the PTO of J_2 to J_4 shows a remarkable 282.88%, 63.02% and 80.23% improvement when the system operated under irregular waves, implying the robustness and adaptability of the control method. The higher values of P_{PTO} under irregular waves validate the control method's efficiency to enhance the power extraction of PTO. In comparison with other objective functions, J_4 demonstrates the second-best performance in enhancing P_{PTO} (80.23%). As stated in previous section, the objective function of J_4 contains multiple time-variant variables, making it difficult to converge. The convergence under J_2 and J_4 is compared in Fig. 29, where J_2 shows a better convergence. Therefore, the power extraction performance under J_2 is better.

The current method can be integrated to the framework of MPC. We

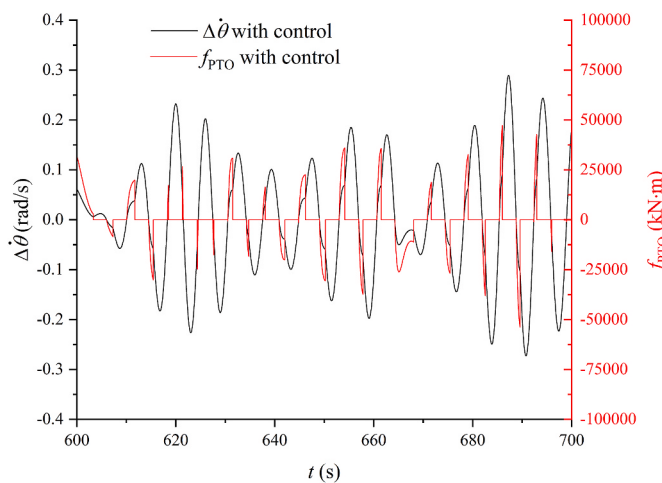


Fig. 27. Time history of the relative rotational velocity and the PTO force.

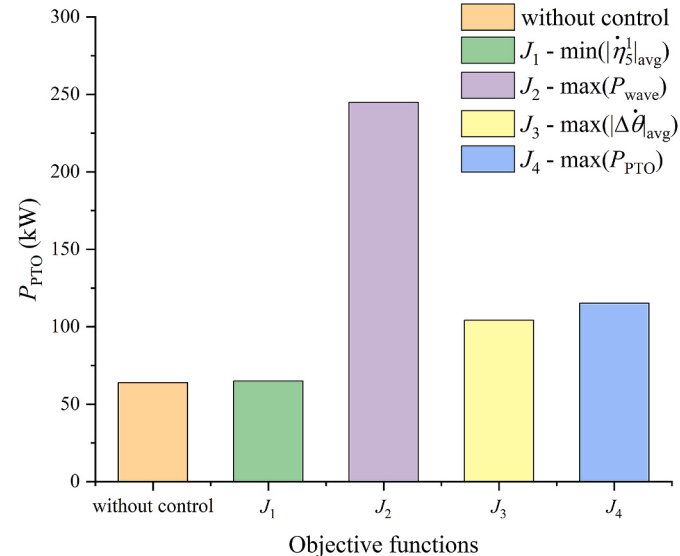


Fig. 28. Comparison of the total power absorbed by PTO.

have considered applying our method in real time in our subsequent research. Within the MPC framework, the control strategy is optimised over a short future time horizon and then applied step-by-step. Our current research focuses solely on the optimisation aspect within a predefined time horizon based on available information, without considering the prediction, particularly due to the complexities involved with managing multiple floating bodies. The issue of non-causality caused by the irregular inputs could be effectively addressed through the prediction of future information (Li et al., 2021).

4.6. Extended discussion of a 3-body system

The model of a hinged 3-body system can be illustrated as a segment

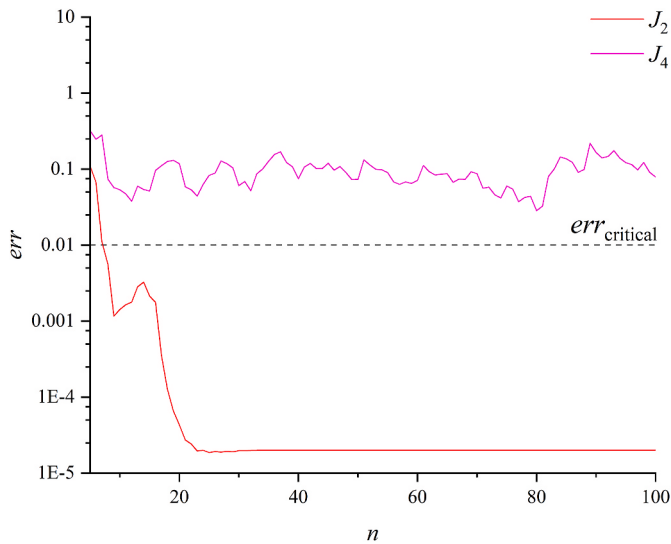


Fig. 29. The convergence of J_2 and J_4 under irregular waves (The err is shown in logarithmic scale).

of Fig. 1. For a 3-body system, the total constraint matrix is the product of the individual constraint matrices. Consequently, the system state matrix can be reformulated as

$$\begin{aligned} \eta = \begin{bmatrix} \eta^1 \\ \eta^2 \\ \eta^3 \end{bmatrix} &= \begin{bmatrix} I & 0 & 0 \\ 0 & I & 0 \\ 0 & S_{21} & S_{22} \end{bmatrix} \begin{bmatrix} \eta^1 \\ \eta^2 \\ \theta^2 \end{bmatrix} = \begin{bmatrix} I & 0 & 0 \\ 0 & I & 0 \\ 0 & S_{21} & S_{22} \end{bmatrix} \begin{bmatrix} I & 0 & 0 \\ S_{21} & S_{22} & 0 \\ 0 & 0 & I \end{bmatrix} \begin{bmatrix} \eta^1 \\ \theta^1 \\ \theta^2 \end{bmatrix} \\ &= \begin{bmatrix} I & 0 & 0 \\ S_{21} & S_{22} & 0 \\ S_{21}S_{21} & S_{21}S_{22} & S_{22} \end{bmatrix} \begin{bmatrix} \eta^1 \\ \theta^1 \\ \theta^2 \end{bmatrix} = S \begin{bmatrix} \eta^1 \\ \theta^1 \\ \theta^2 \end{bmatrix} = S\eta' \end{aligned} \quad (28)$$

The motion equation remains the same form as Eq. (14) with an extended input $f_e(t) = [f_e^1(t), f_e^2(t), f_e^3(t)]^T$ and state vector $\eta'(t) = [\eta^1(t), \theta^1(t), \theta^2(t)]^T$. The input regular waves have the same configuration as Section 4.3. The amplitude of the wave excitation force on *Box_3*, denoted as $f_e^3(t)$, is relatively smaller than those acting on *Box_1* and *Box_2*. The expanded DoF of the 3-body system is 8. Besides, the interactions amongst the three bodies should also be considered in the analysis.

Each pair of adjacent bodies is interconnected by a single PTO unit. Under the assumption that both PTOs have an identical configuration, the total power output of the two units is expressed as follows

$$P_{\text{PTO}} = \frac{1}{T} \int_0^T \left[(B_{\text{PTO}} + \beta^1 B_c) (\Delta \dot{\theta}^1)^2 + (B_{\text{PTO}} + \beta^2 B_c) (\Delta \dot{\theta}^2)^2 \right] dt \quad (29)$$

where β^1 and β^2 is the control command for the PTO between *Box_1* and *Box_2*, while β^2 corresponds to the control command for the PTO between *Box_2* and *Box_3*.

The optimal control for the 3-body system is implemented using objective function J_4 , which represents the maximisation of the total PTO power output in Eq. (29). The control command results are illustrated in Fig. 30. This figure shows that the two PTOs have different control behaviours during the control process, aiming to maximise the overall system performance. Fig. 31 displays the variation of err and P_{PTO} with iteration. The results indicate a slow convergence, yet an overall improvement in performance is observed.

The phase relationship between the PTO force and the relative rotational velocity under declutching control is depicted in Fig. 32. In this figure, the shaded area denotes the power generated by the PTO. The duration in which the PTO force is active and does work is not increased; however, its amplitude is significantly higher, leading to a higher total power output. This observation demonstrates the effective

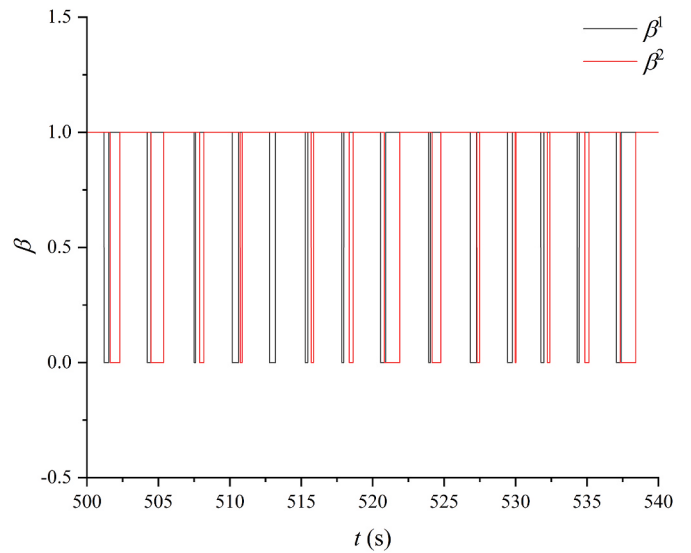


Fig. 30. The control command of 3-body optimal control under J_4 .

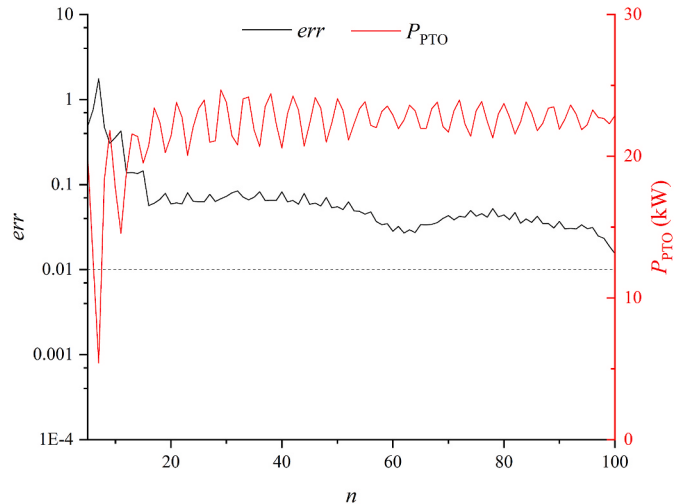


Fig. 31. The variation of err and P_{PTO} with iteration.

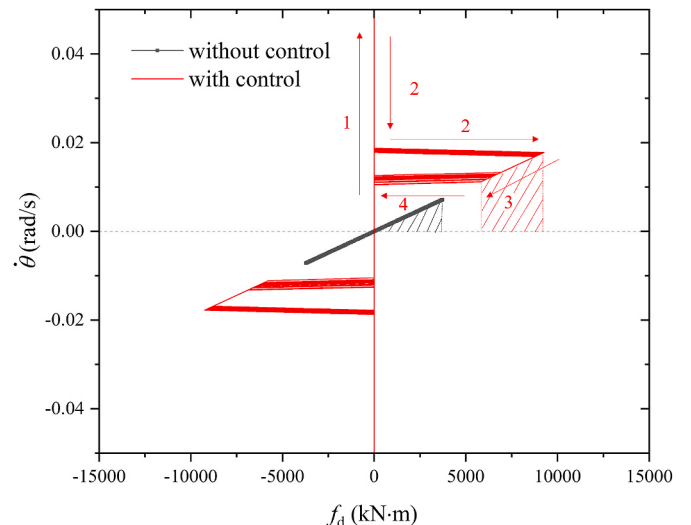


Fig. 32. Phase relationship of the $\dot{\theta}$ and f_d for 3-body system.

expandability of the 3-body system. It indicates that some conclusions drawn from the study of two-hinged box systems remain applicable and valid in this more complex configuration.

5. Conclusion and future work

A novel optimal declutching control method is developed to optimise the performance of floating multiple bodies. This paper takes a hinged box system as a case study to investigate whether the proposed control method can archive the objectives, and evaluate its effectiveness. The hydrodynamic coefficients and wave excitation forces are solved with potential flow theory, while the time domain simulation and the optimal control method, Pontryagin's Maximum Principle, are implemented in MATLAB.

Optimal declutching control can periodically load off the PTO force between bodies in regular waves, tuning the phase between the body velocities and the wave forces. The maximisation or minimisation of performance indices depends on how the objective functions (J) are defined. Results in this paper demonstrate that optimal declutching control can effectively realise the motion reduction of *Box 1* (J_1), the enhancement of the wave power absorption (J_2), the increase of relative angular velocity between boxes (J_3), and the enhancement of PTO power absorption (J_4). The electrical power of the generator, taking into account the loss of the electric generator, is another possible option for J_4 in the future work. The velocity and the force-velocity phase relationship both have a great influence on the control effects, whose weightings are different in different wave frequencies. All objective functions show a better control effect on their respective performance indices than others. The number of iterations is determined by setting a critical error threshold to determine if the computation has converged.

However, the solution of optimising J_4 does not have good convergence as this objective function has multiple time-variant variables that are related to control. Pontryagin's Maximum Principle is possible to experience lengthy iterations and fail to converge to an optimum when the trajectories vary significantly. The main limitation of the proposed control method is that its effect is sensitive to the form of objective functions. It is necessary to try some alternative global optimisation methods, such as simulated annealing, genetic algorithms, particle swarm optimisation, and ant colony optimisation. The results in different wave frequencies indicate that the control effect for certain objective functions, such as J_1 , is sensitive to the wave frequency. The limitation is mainly caused by the wave phase difference between the two boxes. This could potentially be addressed by designing the scale of one box to be much smaller than the other. Besides, future research could include exploring multi-objective control strategies, such as the conflicting objectives of J_1 and J_4 , with Pareto optimality.

Funding

This study was financially supported by the National Natural Science Foundation of China (51979131) and China Scholarship Council Foundation (CSC201806680084).

CRediT authorship contribution statement

Shuang-Rui Yu: Writing – review & editing, Writing – original draft, Software, Methodology, Investigation, Funding acquisition, Formal analysis, Data curation, Conceptualization. **Ming Zhang:** Writing – review & editing, Methodology, Data curation. **De-Qing Zhang:** Writing – review & editing, Validation, Methodology. **Zhi-Ming Yuan:** Writing – review & editing, Supervision, Funding acquisition, Conceptualization.

Declaration of competing interest

The authors declare that they have no known competing financial

interests or personal relationships that could have appeared to influence the work reported in this paper.

Data availability

Data will be made available on request.

References

- Airy, G.B., 1845. *Tides and Waves*. B. Fellowes.
- Babarit, A., Guglielmi, M., Clement, A.H., 2009. Declutching control of a wave energy converter. *Ocean Eng.* 36, 1015–1024. <https://doi.org/10.1016/j.oceaneng.2009.05.006i>.
- Cheng, Z., Gao, Z., Moan, T., 2018. Hydrodynamic load modeling and analysis of a floating bridge in homogeneous wave conditions. *Mar. Struct.* 59, 122–141. <https://doi.org/10.1016/j.marstruc.2018.01.007>.
- Choi, Y.R., Hong, S.Y., 2002. An analysis of hydrodynamic interaction of floating multi-body using higher-order boundary element method. In: The Twelfth International Offshore and Polar Engineering Conference. International Society of Offshore & Polar Engineers.
- Cummins, W.E., 1962. *The Impulse Response Function and Ship Motions*. David Taylor Model Basin, Washington DC.
- Falnes, J., 2002. *Ocean Waves and Oscillating Systems*, 2002. *Linear Interactions Including Wave-Energy Extraction*. Cambridge University Press, Cambridge. ISBN 9780511754630.
- Hals, J., Falnes, J., Moan, T., 2011. A comparison of selected strategies for adaptive control of wave energy converters. *J. Offshore Mech. Arctic Eng.* 133 <https://doi.org/10.1115/1.4002735>.
- Henderson, R., 2006. Design, simulation, and testing of a novel hydraulic power take-off system for the Pelamis wave energy converter. *Renew. Energy* 31, 271–283. <https://doi.org/10.1016/j.renene.2005.08.021>.
- Kashiwagi, M., Endo, K., Yamaguchi, H., 2005. Wave drift forces and moments on two ships arranged side by side in waves. *Ocean Eng.* 32, 529–555. <https://doi.org/10.1016/j.oceaneng.2004.09.005>.
- Li, L., Gao, Y., Ning, D.Z., Yuan, Z.M., 2021. Development of a constraint non-causal wave energy control algorithm based on artificial intelligence. *Renew. Sustain. Energy Rev.* 138 <https://doi.org/10.1016/j.rser.2020.110519>.
- Liu, C., Zhao, Z., Hu, M., Gao, W., Chen, J., Yan, H., Zeng, Y., Zhang, T., Liu, X., Yang, Q., Bao, G., Chen, S., Wei, D., 2022. A novel discrete control for wave energy converters with a hydraulic power take-off system. *Ocean Eng.* 249 <https://doi.org/10.1016/j.oceaneng.2022.110887>.
- Muliawan, M.J., Karimirad, M., Moan, T., 2013. Dynamic response and power performance of a combined Spar-type floating wind turbine and coaxial floating wave energy converter. *Renew. Energy* 50, 47–57. <https://doi.org/10.1016/j.renene.2012.05.025>.
- Newman, J.N., 1994. Wave effects on deformable bodies. *Appl. Ocean Res.* 16, 47–59.
- Noad, I.F., Porter, R., 2017. Modelling an articulated raft wave energy converter. *Renew. Energy* 114, 1146–1159. <https://doi.org/10.1016/J.RENENE.2017.07.077>.
- Perez, T., Fossen, T.I., 2009. A Matlab toolbox for parametric identification of radiation-force models of ships and offshore structures. *Model. Ident. Control* 30, 1–15. <https://doi.org/10.4173/mic.2009.1.1>.
- Ringwood, J.V., Bacelli, G., Fusco, F., 2014. Energy-maximizing control of wave-energy converters: the development of control system technology to optimize their operation. *IEEE Control Syst. Mag.* 34, 30–55. <https://doi.org/10.1109/MCS.2014.2333253>.
- Salter, S.H., Taylor, J.R.M., Caldwell, N.J., 2002. *Power Conversion Mechanisms for Wave Energy*.
- Sun, L., Taylor, R.E., Choo, Y.S., 2011. Responses of interconnected floating bodies. *IES J. Part A Civ. Struct. Eng.* 4, 143–156. <https://doi.org/10.1080/19373260.2011.577933>.
- Yemm, R., Pizer, D., Retzler, C., Henderson, R., 2012. Pelamis: experience from concept to connection. *Phil. Trans. Math. Phys. Eng. Sci.* 370, 365–380. <https://doi.org/10.1098/rsta.2011.0312>.
- Yuan, Z.M., Incevik, A., Dai, S., Alexander, D., Ji, C.Y., Zhang, X., 2015. Hydrodynamic interactions between two ships travelling or stationary in shallow waters. *Ocean Eng.* 108, 620–635. <https://doi.org/10.1016/j.oceaneng.2015.08.058>.
- Zhang, D., Du, J., Yuan, Z., Yu, S., Li, H., 2023. Motion characteristics of large arrays of modularized floating bodies with hinge connections. *Phys. Fluids* 35. <https://doi.org/10.1063/5.0153317>.
- Zhang, D., Yuan, Z.M., Du, J., Li, H., 2022. Hydrodynamic modelling of large arrays of modularized floating structures with independent oscillations. *Appl. Ocean Res.* 129 <https://doi.org/10.1016/j.apor.2022.103371>.
- Zhang, X.-T., Yang, J.-M., Xiao, L.-F., 2014. Declutching control of a point absorber with direct linear electric PTO systems. *Ocean Syst. Eng.* 4, 63–82. <https://doi.org/10.12989/ose.2014.4.1.063>.
- Zheng, S.M., Zhang, Y.H., Zhang, Y.L., Sheng, W.A., 2015. Numerical study on the dynamics of a two-raft wave energy conversion device. *J. Fluid Struct.* 58, 271–290. <https://doi.org/10.1016/j.jfluidstructs.2015.07.008>.
- Zhou, X., Zhang, H., Jin, H., Liu, C., Xu, D., 2023. Numerical and experimental investigation of a hinged wave energy converter with negative stiffness mechanism. *Int. J. Mech. Sci.* 245, 108103 <https://doi.org/10.1016/J.IJMECSCI.2023.108103>.